



UPPSALA  
UNIVERSITET

*Digital Comprehensive Summaries of Uppsala Dissertations  
from the Faculty of Science and Technology 2032*

# Silicon Nanowire Based Electronic Devices for Sensing Applications

QITAO HU



ACTA  
UNIVERSITATIS  
UPSALIENSIS  
UPPSALA  
2021

ISSN 1651-6214  
ISBN 978-91-513-1186-9  
urn:nbn:se:uu:diva-439645

Dissertation presented at Uppsala University to be publicly examined in Polhemsalen, Ångströmlaboratoriet, Lägerhyddsvägen 1, Uppsala, Monday, 31 May 2021 at 14:00 for the degree of Doctor of Philosophy. The examination will be conducted in English. Faculty examiner: Associate Professor Jeehwan Kim (Massachusetts Institute of Technology).

## Abstract

Hu, Q. 2021. Silicon Nanowire Based Electronic Devices for Sensing Applications. *Digital Comprehensive Summaries of Uppsala Dissertations from the Faculty of Science and Technology* 2032. 73 pp. Uppsala: Acta Universitatis Upsaliensis. ISBN 978-91-513-1186-9.

Silicon nanowire (SiNW) based electronic devices fabricated with a complementary metal-oxide-semiconductor (CMOS) compatible process have wide-range and promising applications in sensing area. These SiNW sensors own high sensitivity, low-cost mass production possibility, and high integration density. In this thesis, we design and fabricate SiNW electronic devices with the CMOS-compatible process on silicon-on-insulator (SOI) substrates and explore their applications for ion sensing and quantum sensing.

The thesis starts with ion sensing using SiNW field-effect transistors (SiNWFETs). The specific interaction between a sensing layer and analyte generates a change of local charge density and electrical potential, which can effectively modulate the conductance of SiNW channel. Multiplexed detection of molecular ( $\text{MB}^+$ ) and elemental ( $\text{Na}^+$ ) ions is demonstrated using a SiNWFET array, which is functionalized with ionophore-incorporated mixed-matrix membranes (MMMs). As a follow-up, polyethylene glycol (PEG) doping strategy is explored to suppress interference from the hydrophobic molecular ion and expand the multiplexed detection range. Then, the SiNW is downscaled to sub-10 nm with a gate-oxide-free configuration for single charge detection in liquid. We directly observe the capture and emission of a single  $\text{H}^+$  ion with individually activated Si dangling bonds (DBs) on the SiNW surface. This work demonstrates the unprecedented ability of the sub-10 nm SiNWFET for investigating the physics of the solid/liquid interface at single charge level.

Apart from ion sensing, the SiNWFET can be suspended and act as a nanoelectromechanical resonator aiming for electrically detecting potential quantized mechanical vibration at low temperature. A suspended SiNW based single-hole transistor (SHT) is explored as a nanoelectromechanical resonator at 20 mK. Mechanical vibration is transduced to electrical readout by the SHT, and the transduction mechanism is dominated by piezoresistive effect. A giant effective piezoresistive gauge factor ( $\sim 6000$ ) with a strong correlation to the single-hole tunneling is also estimated. This hybrid device is demonstrated as a promising system to investigate macroscopic quantum behaviors of vibration phonon modes.

Noise, including intrinsic device noise and environmental interference, is a serious concern for sensing applications of SiNW electronic devices. A  $\text{H}_2$  annealing process is explored to repair the SiNW surface defects and thus reduce the intrinsic noise by one order of magnitude. To suppress the external interference, lateral bipolar junction transistors (LBJTs) are fabricated on SOI substrate for local signal amplification of the SiNW sensors. Current gain and overall signal-to-noise ratio of the LBJTs are also optimized with an appropriate substrate voltage.

**Keywords:** silicon nanowire, field-effect transistor, nanoelectromechanical resonator, CMOS-compatible, multiplexed detection, single charge detection, quantum sensing

*Qitao Hu, Department of Electrical Engineering, Solid-State Electronics, Box 534, Uppsala University, SE-751 21 Uppsala, Sweden.*

© Qitao Hu 2021

ISSN 1651-6214

ISBN 978-91-513-1186-9

urn:nbn:se:uu:diva-439645 (<http://urn.kb.se/resolve?urn=urn:nbn:se:uu:diva-439645>)

*To my beloved family*



# List of Papers

This thesis is based on the following papers, which are referred to in the text by their Roman numerals.

- I     Chen X.\*, **Hu Q.\***, Chen S., Netzer N. L., Wang Z., Zhang S.-L. & Zhang Z. (2018) Multiplexed Analysis of Molecular and Elemental Ions Using Nanowire Transistor Sensors. *Sensors and Actuators B: Chemical*, 270, 89–96.
- II    **Hu Q.**, Chen S., Wang Z. & Zhang Z. (2021) Improving Selectivity of Ion-Sensitive Membrane by Polyethylene Glycol Doping. *Sensors and Actuators B: Chemical*, 328, 128955.
- III   **Hu Q.**, Chen S., Solomon P. & Zhang Z. (2021) Single Charge Detection in Liquid Sample Using Sub-10 nm Silicon Nanowire Transistors. *Submitted to Nature Electronics*.
- IV   Zhang Z.-Z.\*, **Hu Q.\***, Song X.-X., Ying Y., Li H.-O., Zhang Z. & Guo G.-P. (2020) A Suspended Silicon Single-Hole Transistor as an Extremely Scaled Gigahertz Nanoelectromechanical Beam Resonator. *Advanced Materials*, 32(52), 2005625.
- V     **Hu Q.\***, Chen X.\*, Norström H., Zeng S., Liu Y., Gustavsson F., Zhang S.-L., Chen S. & Zhang Z. (2018) Current Gain and Low-Frequency Noise of Symmetric Lateral Bipolar Junction Transistors on SOI. In *48th European Solid-State Device Research Conference (ESSDERC)*, 258–261.
- VI    **Hu Q.**, Chen S., Zhang S.-L., Solomon P. & Zhang Z. (2020) Effects of Substrate Bias on Low-Frequency Noise in Lateral Bipolar Transistors Fabricated on Silicon-on-Insulator Substrate. *IEEE Electron Device Letters*, 41(1), 4–7.

\*The authors contributed equally to the work. Reprints were made with permission from the respective publishers.

# Author's Contributions

- I Performed the MMM preparation and ion sensing measurements, and wrote part of the manuscript.
- II Planned and performed the MMM preparation, ISE fabrication and characterization, and ion sensing measurements, and wrote the manuscript.
- III Planned and performed the device fabrication and characterization, ion sensing measurements, and modeling, and wrote the manuscript.
- IV Planned and performed the device fabrication and TCAD simulation, and wrote part of the manuscript.
- V Performed most work of the device fabrication, and wrote part of the manuscript.
- VI Planned and performed the device fabrication and characterization, and wrote the manuscript.

## List of Papers Not Included in the Thesis

- I     Chen X., Chen S., **Hu Q.**, Zhang S.-L., Solomon P. & Zhang Z. (2019) Device Noise Reduction for Silicon Nanowire Field-Effect-Transistor Based Sensors by Using a Schottky Junction Gate. *ACS Sensors*, 4, 427–433.
- II    Tseng C.-W., Wen C., Huang D.-C., Lai C.-H., Chen S., **Hu Q.**, Chen X., Xu X., Zhang S.-L., Tao Y.-T. & Zhang Z. (2020) Synergy of Ionic and Dipolar Effects by Molecular Design for pH Sensing beyond the Nernstian Limit. *Advanced Science*, 7(2), 1901001.
- III    Chen S., Luo C., Zhang Y., Xu J., **Hu Q.**, Zhang Z. & Guo G. (2020) Current Gain Enhancement for Silicon-on-Insulator Lateral Bipolar Junction Transistors Operating at Liquid-Helium Temperature. *IEEE Electron Device Letters*, 41(6), 800–803.
- IV    Yu Y., Chen S., **Hu Q.**, Solomon P. & Zhang Z. (2021) Ultra-Low Noise Schottky Junction Tri-Gate Silicon Nanowire FET on Bonded Silicon-on-Insulator Substrate. *IEEE Electron Device Letters*, 42(4), 469–472.
- V     Xu X., Yu Y., **Hu Q.**, Chen S., Nyholm L. & Zhang Z. (2021) Surface Redox Buffering Effects on Potentiometric Detection of DNA Using Gold Substrates. *Resubmitted to ACS Sensors*.





# Contents

1. Introduction.....	15
1.1 Background .....	15
1.2 Thesis organization .....	18
2. Fundamentals .....	19
2.1 SiNWFET sensor.....	19
2.2 SiNW resonator sensor.....	23
2.3 Noise of SiNW device.....	24
3. Fabrication and Characterization of SiNW Devices .....	26
3.1 CMOS-compatible fabrication .....	26
3.2 Process optimization .....	28
3.3 Electrical characterization .....	29
4. Multiplexed Ion Detection Using SiNWFET Array .....	30
4.1 Working principle of MMM.....	30
4.2 Multiplexed detection of molecular and elemental ions.....	32
4.3 PEG doping for improving ion selectivity .....	34
5. Single Charge Detection in Liquid Using Sub-10 nm SiNWFETs.....	38
5.1 Direct observation of single $H^+$ -DB interaction .....	38
5.2 Single $H^+$ -DB interaction analysis.....	42
5.3 One-by-one activation of DBs.....	47
6. SiNW Resonator for Quantum Sensing .....	49
6.1 3 GHz SiNW resonator.....	49
6.2 Single-hole transistor behavior.....	51
6.3 Transduction mechanism analysis.....	52
7. Lateral BJTs as Local Signal Amplifiers .....	55
7.1 Device fabrication and characterization .....	55
7.2 Substrate voltage modulation .....	56
8. Conclusions and Future Perspectives.....	60

Sammanfattning på Svenska .....	63
Acknowledgement .....	65
References .....	67

# Abbreviations

ALD	Atomic layer deposition
B	Base
BJT	Bipolar junction transistor
BOX	Buried oxide
C	Collector
CEA	Carcinoembryonic antigen
CMOS	Complementary metal-oxide-semiconductor
D	Drain
DB	Dangling bond
DI	Deionized
E	Emitter
EBL	Electron beam lithography
EDL	Electrical double layer
FET	Field-effect transistor
FGA	Forming gas annealing
HF	Hydrofluoric acid
HSQ	Hydrogen silsesquioxane
ISE	Ion-selective electrode
LBJT	Lateral bipolar junction transistor
mAbs	Monoclonal antibodies
MB	Methylene blue
MMM	Mixed-matrix membrane
MOSC	Metal-organic supercontainer
MOSFET	Metal-oxide-semiconductor field-effect transistor
PEG	Polyethylene glycol
PSA	Prostate specific antigen
PSD	Power spectrum density
PVC	Polyvinyl chloride
RE	Reference electrode
RIE	Reactive ion etching
RTN	Random telegraph noise
RTP	Rapid thermal processing

S	Source
SCR	Space charge region
SEM	Scanning electron microscope
SHT	Single-hole transistor
SiNW	Silicon nanowire
SNR	Signal-to-noise ratio
SOI	Silicon-on-insulator
SS	Subthreshold slope
THF	Tetrahydrofuran
XTEM	Cross-sectional transmission electron microscope
$A$	Gating area
$c_{\text{Hb}}$	$\text{H}^+$ concentration in bulk solution
$c_{\text{HCl}}$	HCl concentration
$c_{\text{Hs}}$	$\text{H}^+$ concentration at surface
$c_{\text{K}}$	$\text{K}^+$ concentration
$c_{\text{liq}}$	Target ion concentration in the liquid
$c_{\text{MB}}$	$\text{MB}^+$ concentration
$c_{\text{Na}}$	$\text{Na}^+$ concentration
$C_{\text{EDL}}$	Electrical double layer capacitance
$C_{\text{dif}}$	Diffuse layer capacitance
$C_{\text{OX}}$	Gate oxide capacitance
$C_{\text{Si}}$	Silicon nanowire capacitance
$C_{\text{st}}$	Stern layer capacitance
$E$	Young's modulus
$E_{\text{PB}}$	Phase boundary potential
$E_{\text{WE}}$	Working electrode potential
$f_0$	Resonant frequency
$f_c$	Corner frequency
$f_d$	Driven frequency
$f_{\text{shift}}$	Shift of resonance peak
$f_{\text{width}}$	Width of resonance peak
$g$	Gauge factor
$g_{\text{m}}$	Transconductance
$G$	Conductance
$I_{\text{B}}$	Base current
$I_{\text{C}}$	Collector current
$I_{\text{C-B}}$	Collector current in silicon bulk

$I_{C-I}$	Collector current at silicon/buried oxide interface
$I_{DS}$	Drain-to-source current
$I_G$	Gate leakage current
$I_{mix}$	Mixed current
$I_{mix}^{FET}$	Mixing current at resonance based on field-effect
$I_{mix}^{PZT}$	Mixing current at resonance based on piezoresistive effect
$I_{mix}^{res}$	Mixing current at resonance
$h$	Plank constant
$k$	Boltzmann constant
$k_{off}$	Dissociation constant
$k_{on}$	Association constant
$K_{Na, MB}$	Selectivity coefficient of $Na^+$ -sensor against $MB^+$
$L$	Silicon nanowire length
$m_{eff}$	Effective mass of resonator
$n_{ph}$	Thermal phonon occupancy
$N$	Carrier number
$N_A$	Acceptor concentration
$N_D$	Donor concentration
$N_t$	Trap density in volume
$pH_s$	Surface $pH$
$pH_b$	Bulk liquid $pH$
$P$	Occupation probability of dangling bond
$P_d$	Driving power
$q$	Elemental charge
$Q$	Quality factor
$S_{IB}$	Base current noise power spectrum density
$S_{IC}$	Collector current noise power spectrum density
$S_{ID}$	Drain current noise power spectrum density
$S_{VG}$	Gate-referred voltage noise power spectrum density
$t_c$	Capture time
$t_e$	Emission time
$T$	Temperature
$V_B$	Base voltage
$V_C$	Collector voltage
$V_D$	Drain voltage
$V^{FM}(t)$	Frequency-modulation signal

$V_G$	Gate voltage
$V_{st}$	Electrical potential across Stern layer
$V_{sub}$	Substrate voltage
$V_T$	Threshold voltage of field-effect transistor
$W$	Silicon nanowire width
$W_B$	Base width
$x$	Displacement of resonator
$x_{zp}$	Zero-point displacement of resonator
$\alpha_{sc}$	Coulomb scattering coefficient
$\alpha_t$	Tunneling coefficient of electrons
$\beta$	Current gain
$\beta_{int}$	Intrinsic buffer capacity
$\theta$	Fraction of bound receptor
$\mu$	Carrier mobility
$\mu_D$	Fermi level in drain
$\mu_{QD}$	Electrochemical potential of quantum dot
$\mu_S$	Fermi level in source
$\tau_c$	Capture time constant
$\tau_e$	Emission time constant
$\rho$	Mass density
$\varphi_s$	Surface potential in solid/liquid interface
$\psi_s$	Surface potential in semiconductor
$\Delta E_{cap}$	Kinetic energy barriers of capture process
$\Delta E_{emi}$	Kinetic energy barriers of emission process

# 1. Introduction

## 1.1 Background

The senses of light, smell, taste, touch, and hearing are the fundamental and indispensable mechanisms, through which humans obtain information from their surroundings for survival. Sensors, artificial sensing organs, are devices that can detect physical and chemical properties and changes of these properties in environment and then transfer them into human-readable signals [1], [2]. These physical and chemical properties include temperature [3], pressure [4], humidity [5],  $pH$  [6], concentrations of concerned chemical species [7]-[9], *etc.* The signal generation of a sensor can be based on electrical [10], mechanical [11], optical [12], or electrochemical [13] mechanisms.

The wide usage of sensors will change our daily life to a large extent. For example, a precise and real-time monitoring of harmful and hazardous chemical and biological substances guards the whole society running in a healthy and secure status. Such substances could be heavy metal ions [14] and antibiotics molecules [15] in river and lake, as well as explosive gases [16] and environmental pollutants [17] generated in industrial production. Highly sensitive and accurate detection and analysis of specific biomarkers can not only provide much information about one's physiological state, but also play an important role in early diagnosis, which greatly increases the chance of curing a disease [18], [19]. In addition, network integrated with multiple sensors can serve as one of the basic architectures for Internet of Things [20]. Efficient information delivery and communication of the sensor network lead to an intelligent home and city.

The advance of nanofabrication techniques has recently led to tremendous development of nanoelectronics sensors. Those sensors have attracted great interest due to their capability of label-free, fast, and real-time sensing [21]-[23]. Besides, the possibility of low-cost fabrication and miniaturization further promotes the applications of nanoelectronics sensors and their integration with external signal process schemes.

Silicon nanowire (SiNW) based field-effect transistor (FET) sensors are one category of emerging and powerful nanoelectronics sensors [24]. They have been widely studied in the label-free, sensitive, and multiplexed detection of analytes ranging from elemental ions [25]-[27], biomolecules [28]-[30], and gases [31], [32]. In the SiNWFET, gate oxide surface on the SiNW channel can be functionalized with a receptor-incorporated sensing

layer. Once the charged target is captured by the sensing layer, the induced change of local potential will modulate SiNW channel conductance and produce a readout current signal.

SiNWFET arrays can be integrated on a single chip and be selectively functionalized, which enables the simultaneous detection and analysis of multiple targets [33]-[35]. Multiplexed detection could greatly improve throughput and efficiency. As illustrated in Figure 1.1, label-free and multiplexed electrical detection of three cancer markers was demonstrated by G. Zheng *et al.* using an array of three SiNWFET sensors [36]. Monoclonal antibodies (mAbs) of three cancer biomarkers, *i.e.*, prostate specific antigen (PSA), carcinoembryonic antigen (CEA), and mucin-1, were selectively immobilized on the gate surface of each sensor. These SiNWFET sensors exhibited a high selectivity towards different analytes, indicated by their negligible responses to the non-specific analytes.

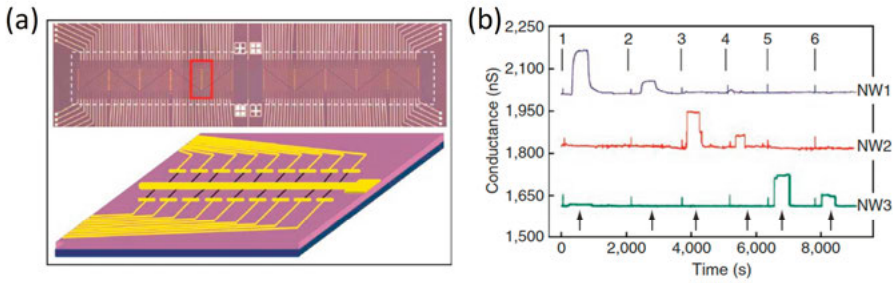
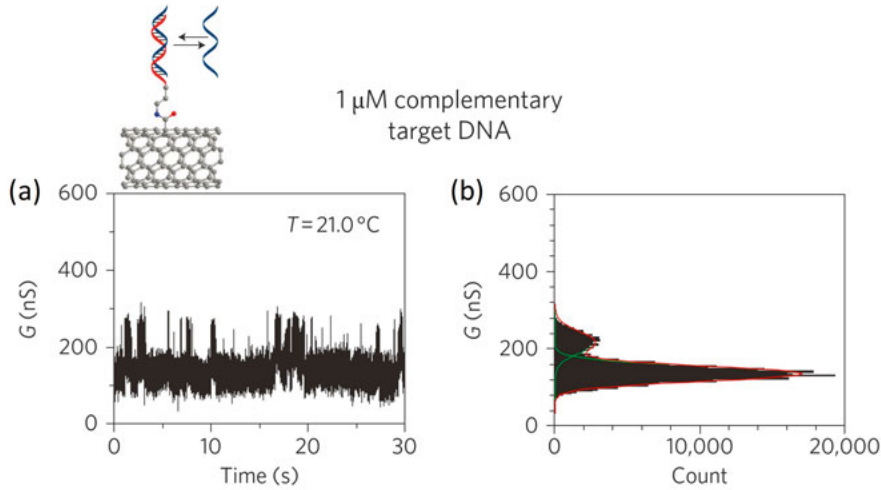


Figure 1.1. (a) Optical image (top) and schematic (bottom) of the SiNWFET array. (b) Conductance response data recorded for the simultaneous detection of PSA, CEA, and mucin-1 using the SiNWFET array. NW 1, NW 2, and NW 3 were functionalized with mAbs for PSA, CEA, and mucin-1, respectively. The solutions were delivered to the SiNWFET array sequentially as follows: (1) 0.9 ng/ml PSA, (2) 1.4 pg/ml PSA, (3) 0.2 ng/ml CEA, (4) 2 pg/ml CEA, (5) 0.5 ng/ml mucin-1, and (6) 5 pg/ml mucin-1. Buffer solutions were injected after each protein solution indicated by the black arrows. Reprinted with permission from [36]. Copyright (2005) Springer Nature.

Another advantage of SiNWFET is the enhanced charge sensitivity by scaling down SiNW dimensions, which can potentially reach single charge resolution [37]-[39]. Recently, direct detection of single DNA molecule was realized by S. Sorgenfrei *et al.* using a carbon nanotube (CNT) based transistor [40], [41]. As shown in Figure 1.2, one probe DNA was decorated on the CNT surface, which could capture and emit a single complementary DNA in liquid sample. The capture and emission events modulated the CNT channel conductance and generated the conductance switching signal between distinct states. Such approach opened up a novel technique to analyze the DNA hybridization kinetics in addition to statistical methods. However, the complexity of CNT



device fabrication and its difficulty in the integration with external circuits limit its applications [42]. Besides, one DNA molecule usually holds multiple charges [43], which means that the single charge detection is still to be achieved.



*Figure 1.2. (a) Conductance recording of the carbon nanotube transistor with the DNA probe exposed to its complementary DNA target. (b) Conductance based histogram of time intervals. Reprinted with permission from [40]. Copyright (2011) Springer Nature.*

Besides ion sensing, SiNWFET can be suspended and act as a nanoelectromechanical resonator. This hybrid device provides an ideal platform for electrically detecting quantized mechanical vibration and investigating macroscopic quantum behaviors at low temperature [44]. In such device, mechanical vibration can be coupled with carrier transport via capacitive or piezoresistive effects. When SiNW dimensions are downscaled to be comparable with the wavelength of carriers, the separation of energy level of carriers can be larger than the thermal energy, which makes quantum effects of carrier transport visible [45]. In addition, mechanical vibration of the hybrid device can also be quantized at certain temperature [46]. Such device with quantized mechanical vibration can be used for investigating macroscopic quantum behaviors. The quantum behaviors of mechanical vibration have been demonstrated in cavity opto-/electro-mechanical systems [47] and hybrid quantum acoustic system composing superconducting qubits and surface/bulk acoustic wave resonators [48]. However, for future real-world applications, electrical accessibility to mechanical vibration is still desired.

## 1.2 Thesis organization

The main focus of this thesis is to investigate SiNW based transistors and resonators for sensing applications. Chapter 2 introduces the fundamentals about ion sensing, quantum sensing, and noise of SiNW electronic devices. Chapter 3 presents the optimization of CMOS-compatible fabrication process to shrink the SiNW dimensions and suppress the intrinsic device noise. Chapter 4 summarizes the multiplexed detection of methylene blue ( $\text{MB}^+$ ) and sodium ( $\text{Na}^+$ ) ions using a SiNWFET array functionalized with mixed-matrix membranes (MMMs). Chapter 5 focuses on the detection of single hydrogen ion ( $\text{H}^+$ ) in liquid using sub-10 nm SiNWFETs with gate-oxide-free configuration. Chapter 6 shows a 3 GHz SiNW resonator aiming for quantum sensing. Chapter 7 introduces lateral BJTs as local signal amplifiers of SiNW sensors for an improved overall signal-to-noise ratio (SNR).

A brief summary of the papers listed in this thesis is presented as following. In **Paper I**, a SiNWFET array is selectively functionalized with ionophore-incorporated MMMs and multiplexed detection of molecular ( $\text{MB}^+$ ) and elemental ( $\text{Na}^+$ ) ions is demonstrated. Hydrophobic interaction between  $\text{MB}^+$  and matrix of the  $\text{Na}^+$ -MMM generates interference to the  $\text{Na}^+$  sensing and limits the multiplexed detection range. To address this issue, **Paper II** uses hydrophilic polyethylene glycol (PEG) doping to reduce the matrix hydrophobicity and thereby to suppress the hydrophobic  $\text{MB}^+$ -matrix interaction. As a result, selectivity of the PEG-doped  $\text{Na}^+$ -MMM against  $\text{MB}^+$  is improved and the multiplexed detection range is expanded by more than one order of magnitude. **Paper III** presents a direct detection and comprehensive analysis of single charge ( $\text{H}^+$ ) in liquid sample using sub-10 nm gate oxide free SiNWFETs. The unprecedented ability of the sub-10 nm SiNWFET is demonstrated for investigating the physics of solid/liquid interface at single charge level. **Paper IV** exhibits a SiNW resonator with a resonant frequency of 3 GHz, which is the highest value among the resonators based on Si-contained materials. The signal transduction is dominated by piezoresistive effect, and the effective piezoresistive gauge factor ( $\sim 6000$ ) extracted from the device ranks among the largest ones of Si. In **Paper V** and **Paper VI**, lateral version of BJTs are designed and fabricated as local current amplifiers for SiNW sensors. A current gain of 70 is realized with 50-nm-wide base region. Substrate voltage modulation effect is systematically studied to improve both current gain and overall SNR.

## 2. Fundamentals

This chapter introduces the fundamentals about ion sensing based on SiNWFETs and quantum sensing based on SiNW resonators. Chapter 2.1 illustrates working principle of ion sensing, including single charge detection, using SiNWFET sensors. Quantum sensing using SiNW resonators is discussed in Chapter 2.2. Intrinsic device noise and environmental interference are discussed in Chapter 2.3.

### 2.1 SiNWFET sensor

A conventional metal-oxide-semiconductor field-effect transistor (MOSFET) is a three-terminal device, consisting of source (S), drain (D), and channel regions. Figure 2.1(a) depicts the schematic of MOSFET fabricated on silicon-on-insulator (SOI) substrate, which consists of top Si, buried oxide (BOX), and bulk Si. Drain-to-source current ( $I_{DS}$ ) flows through the semiconductor channel driven by the voltage applied on D ( $V_D$ ). A gate oxide layer is formed on the semiconductor channel separating it from gate metal. The voltage applied on the gate ( $V_G$ ) generates a vertical electric field in the channel, which bends the energy band and tunes the carrier density. Consequently, the conductance ( $G$ ) of semiconductor channel is modulated by  $V_G$ .

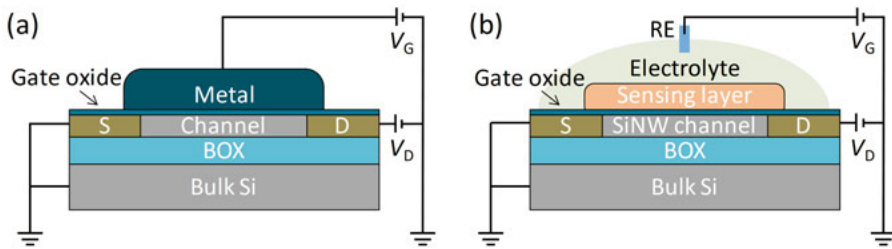


*Figure 2.1. Schematics of (a) MOSFET and (b) SiNWFET sensor fabricated on SOI substrates.*

The structure of a SiNWFET ion-sensitive sensor is similar to that of MOSFET, with the gate metal replaced with an electrolyte (see Figure 2.1(b)).  $V_G$  is applied to the electrolyte via a reference electrode (RE). The gate oxide surface is normally functionalized with a sensing layer incorporated with the

specific receptor, which can selectively interact with the analyte molecule or ion in the electrolyte. Different types of receptors are designed for different targets based on their specific binding mechanisms. For example, the receptor of ion, ionophore, is usually designed with a cavity structure which can bind the target ion with a similar size [49], [50]. The receptor of single-strand DNA is its complementary counterpart [51]. The analyte-receptor interaction on the gate oxide surface can generate a variation of local charge density, leading to a change of surface potential ( $\Delta\varphi_s$ ) and consequently a shift of threshold voltage ( $\Delta V_T$ ) of the SiNWFET. Provided the electrolyte potential is fixed by the RE,  $\Delta V_T$  is then transduced to a change of  $I_{DS}$  by the SiNWFET.

Typically, the sensing surface can be prepared with two approaches. One is to covalently conjugate the receptor molecule on the gate oxide surface [26], [29]. The other one is to coat a polymer membrane incorporated with the receptor molecule on the gate surface [52], [53]. Potentiometric responses to analyte of both methods are based on the same mechanism. Herein,  $pH$  response of the gate oxide surface is used as an example to illustrate the sensing mechanism [54]. When an oxide surface is in contact with electrolyte, an electrical double layer (EDL) forms at the solid/liquid interface (see Figure 2.2) [55].  $-OH$  groups on the oxide surface are the receptors of  $H^+$  and generate  $pH$  responses. The dynamic equilibrium between the  $-OH$  group and surface  $H^+$  can buffer the change of surface  $pH$  ( $pH_s$ ). Since  $pH$  is correlated to electrical potential by the Nernst equation [56], the intrinsic buffer capacity ( $\beta_{int}$ ) of the oxide surface is equivalent to a capacitance, which is connected to EDL capacitance ( $C_{EDL}$ ) in series. Once the bulk  $pH$  ( $pH_b$ ) is changed, the equivalent change of electrical potential will be shared by the equivalent capacitance of  $\beta_{int}$  and  $C_{EDL}$ . The change of  $\varphi_s$ , which corresponds to the potential shared by EDL, can be expressed as [57]

$$\frac{\Delta\varphi_s}{\Delta pH_b} = -2.3\alpha \frac{kT}{q}, \text{ with } \alpha = \frac{1}{\frac{2.3kTC_{EDL}}{q^2\beta_{int}} + 1}, \quad (2.1)$$

where  $k$  is the Boltzmann constant,  $T$  the temperature, and  $q$  the elemental charge. For an oxide surface with an infinitely large  $\beta_{int}$ ,  $\alpha = 1$  and Eq. (2.1) is written as

$$\frac{\Delta\varphi_s}{\Delta pH_b} = -2.3 \frac{kT}{q}. \quad (2.2)$$

This means that for one order of magnitude change of bulk  $H^+$  concentration, the surface potential response  $\Delta\varphi_s$  is  $2.3kT/q = 59.2$  mV at room temperature. Theoretically, 59.2 mV/dec is the maximum potential response for monovalent ions, which is called Nernstian response [57].

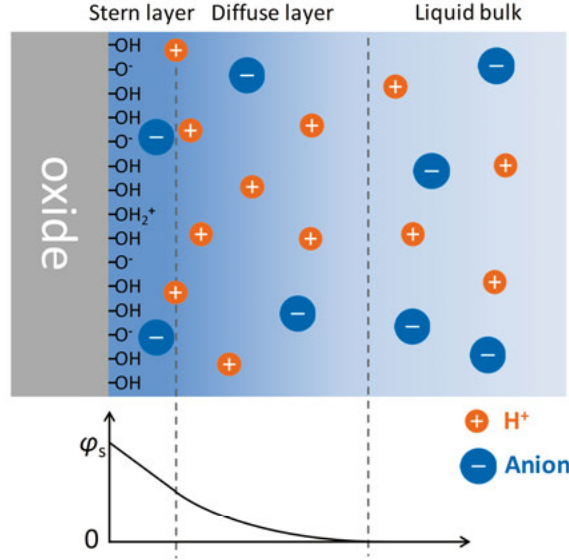


Figure 2.2. Schematic of EDL at oxide/electrolyte interface with the potential distribution across EDL.

With the advancement of Si nanofabrication technology, the width and height of the SiNW channel can be extremely downscaled to, *e.g.*, sub-10 nm [58]. This leads to a much improved charge sensitivity and makes it potentially able to detect a single charge. However, two other technical prerequisites have to be satisfied to achieve the single charge detection using the SiNWFET. First, the intrinsic device noise of such SiNWFET needs to be suppressed to enhance SNR [37], which will be discussed in Chapter 2.3. Second, the number of activated receptors functionalized on the SiNW surface should be small preferably just one, otherwise the signal will be an ensemble response averaged from multiple receptors [39], [40].

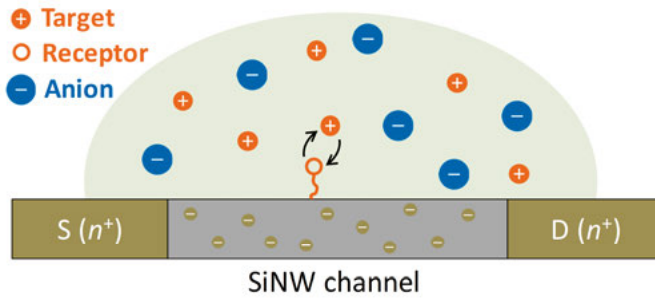


Figure 2.3. Schematic of single charge detection using an n-type SiNWFET.

As indicated in Figure 2.3 and 2.4(a), the single charge captured and emitted by the receptor on the SiNW channel effectively modulates the channel

conductance and generates  $I_{DS}$  switching between distinct levels. The conductance modulation by the single charge can be ascribed to two origins, *i.e.*, number fluctuation ( $\Delta N$ ) and mobility fluctuation ( $\Delta\mu$ ) [59]. For number fluctuation, when the single charge is captured by the receptor on SiNW surface, it is shared by the SiNW capacitance and EDL capacitance [60]. Consequently, carrier number in the SiNW channel is altered. For mobility fluctuation, the captured charge changes local Coulomb scattering strength and modulates carrier mobility in the SiNW channel [61]. The relative amplitude of  $I_{DS}$  switching can be expressed as [62]

$$\frac{\Delta I_{DS}}{I_{DS}} = \frac{\Delta N}{N} + \frac{\Delta\mu}{\mu}. \quad (2.3)$$

Capture ( $\tau_c$ ) and emission ( $\tau_e$ ) time constants characterize the interaction kinetics between the single charge and its receptor. If the capture event of the single charge leads to  $I_{DS}$  switching to a high-state, the period when  $I_{DS}$  stays at a low-state is determined by the probability of capture event. Therefore, the time of low-state is regarded as the capture time ( $t_c$ ) (see Figure 2.4(a)). Correspondingly, the emission time ( $t_e$ ) is the time when  $I_{DS}$  remains at the high-state. The time constants  $\tau_c$  and  $\tau_e$  are defined as the mean values of  $t_c$  and  $t_e$ , respectively.

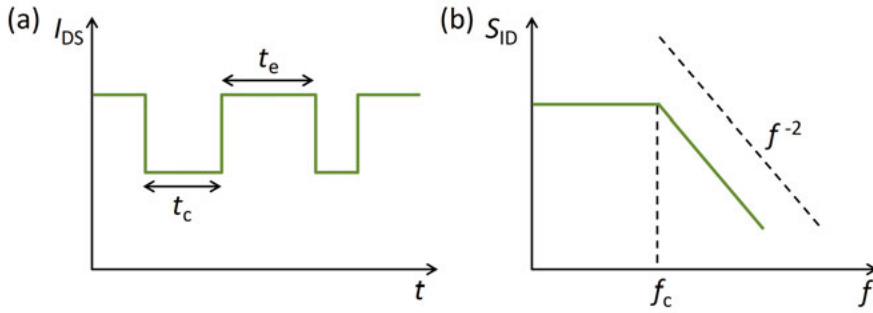


Figure 2.4. (a)  $I_{DS}$  switching signal and (b) its PSD detected by SiNWFET.

$I_{DS}$  switching signal due to the single charge capture/emission events can also be analyzed in frequency domain. As shown in Figure 2.4(b), a typical power spectrum density (PSD) of  $I_{DS}$  switching signal gives a Lorentzian-shape distribution. The corner frequency of PSD ( $f_c$ ) is determined by the time constants [63]:

$$f_c = \frac{1}{2\pi} \left( \frac{1}{\tau_c} + \frac{1}{\tau_e} \right). \quad (2.4)$$

## 2.2 SiNW resonator sensor

The SiNWFET can be suspended and act as a doubly clamped nanoelectromechanical resonator, which provides an ideal platform for electrical detection of potential quantized mechanical vibration at low temperature. In such device, the vibration of SiNW, which is activated by an external electrical field applied from a side gate, could induce extra strain in it and therefore modulate the SiNW conductance via capacitive or piezoresistive effects. The resonant frequency ( $f_0$ ) is determined by the dimensions and mechanical properties of SiNW [64]:

$$f_0 = 1.05 \sqrt{\frac{E}{\rho}} \frac{W}{L^2}, \quad (2.5)$$

where  $E$  is the Young's modulus,  $\rho$  the mass density,  $W$  the SiNW width, and  $L$  the SiNW length.

For the demonstration of quantized mechanical vibration and the real applications, the SiNW resonator has to fulfill the following requirements:

1) Mechanical vibration occupancy reaches its quantum ground state and is well decoupled from thermal environment. A straightforward way is to use a gigahertz mechanical resonator with a high quality factor ( $Q$ ) in milli-kelvin range. Thermal vibration phonon occupancy ( $n_{\text{ph}}$ ) depends on the resonant frequency and the temperature [65]:

$$n_{\text{ph}} = \frac{1}{(e^{hf_0/kT} - 1)}, \quad (2.6)$$

where  $h$  is the Planck constant. For example,  $n_{\text{ph}}$  of the mechanical resonator with a resonant frequency of 1 GHz is estimated to be only  $\sim 0.1$  at 100 mK, which is much below the quantum limit of 1. A high  $Q$  of the vibration is also desired to decouple the mechanical vibration from its thermal environment, *i.e.*,  $f_0 Q \gg kT/h$  ( $f_0 Q$  product reflects the isolation between resonant system and its thermal environment) [66].

2) Effective mass ( $m_{\text{eff}}$ ) of the resonator has to be sufficiently small to ensure an observable zero-point motion ( $x_{\text{zp}}$ ), since  $x_{\text{zp}}$  is given by [67]

$$x_{\text{zp}} = \sqrt{\frac{h}{8\pi^2 f_0 m_{\text{eff}}}}. \quad (2.7)$$

3) A proper detector, which is capable of electrical readout of the quantized mechanical vibration, has to be integrated with the resonator. A commonly used detector is another quantum system (usually a two-level quantum system)

[48], and it detects the mechanical vibration through direct interaction with the resonator.

By downscaling the SiNW dimensions, both a high resonant frequency and a small effective mass can be obtained, which is beneficial for quantizing the mechanical vibration of SiNW resonator.

## 2.3 Noise of SiNW device

Noise is a critical issue for sensing applications when we pursue a high SNR. Both intrinsic device noise and environmental interference of the SiNW devices are addressed in this thesis.

Since the SiNW resonator studied in this thesis is fabricated by suspending a SiNWFET, its intrinsic device noise can be illustrated with the same theory of SiNWFET. The intrinsic noise of SiNWFET is dominated by the random carrier trapping/detrapping processes near SiNW/gate oxide interface [68], which can be explained by the well-established noise models of MOSFET. Typically, intrinsic noise of MOSFET shows a  $1/f$ -like spectrum in the frequency domain. There are two models to explain the physical origin of the  $1/f$  noise of MOSFET, *i.e.*, carrier number fluctuation ( $\Delta N$ ) and carrier mobility fluctuation ( $\Delta\mu$ ) [69]. In  $\Delta N$  model, the traps in the vicinity of the channel/gate oxide interface can randomly trap/detrapp carriers in the channel, which leads to the carrier number fluctuation.  $\Delta\mu$  model associates the  $1/f$  noise to the carrier mobility fluctuation due to the Coulomb scattering near the channel/gate oxide interface. Both  $\Delta N$  and  $\Delta\mu$  models predict a  $1/f$ -like spectrum and they can be combined to a unified model, in which the gate-referred voltage noise ( $S_{VG}$ ) can be expressed as [69]

$$S_{VG} = \frac{q^2 k T N_t}{A C_{OX}^2 \alpha_t f} \left( 1 + \alpha_{sc} \mu C_{OX} \frac{I_{DS}}{g_m} \right)^2, \quad (2.8)$$

where  $N_t$  is the trap density in volume,  $A$  the gate area,  $C_{OX}$  the gate oxide capacitance,  $\alpha_t$  the tunneling coefficient of carriers in the gate oxide,  $\alpha_{sc}$  the Coulomb scattering coefficient, and  $g_m$  the transconductance. As shown in Eq. (2.8),  $S_{VG}$  of the SiNWFET depends on the trap density  $N_t$  near the SiNW/gate oxide interface.  $S_{VG}$  also increases with the reduction of gate area  $A$ , suggesting that the intrinsic noise will become a more severe concern when the SiNW dimensions are downscaled. To address such problem, one strategy is to improve the SiNW surface quality and reduce  $N_t$  near the SiNW/gate oxide interface [70].

Apart from the intrinsic device noise, environmental interference is another concern for overall SNR of electronic sensors. The SiNW electronic sensor is more vulnerable to the environmental interference, since it operates at low



current level. To suppress the external interference, local current amplification using a bipolar junction transistor (BJT) can be a promising solution [71].

### 3. Fabrication and Characterization of SiNW Devices

SiNW electronic devices studied in this thesis are fabricated on SOI wafers using a CMOS-compatible process. In Chapter 3.1, a base fabrication process is introduced. In order to downscale the SiNW to sub-10 nm and suppress the intrinsic device noise, double-exposure and H<sub>2</sub> annealing processes are then developed in Chapter 3.2. Finally, the electrical characteristics of the SiNWFETs are presented in Chapter 3.3.

#### 3.1 CMOS-compatible fabrication

SiNW electrical devices can be fabricated by two approaches: bottom-up and top-down. The bottom-up approach is based on self-assembly growth mechanism. Although as-fabricated SiNWs show a surface with a low defect density, their dimensions are difficult to control and subsequent device fabrication and process integration are challenging. In this thesis, the SiNW devices are fabricated by the top-down approach which is fully CMOS-compatible, *i.e.*, the SiNW pattern is defined by lithography and reactive ion etching (RIE) on a SOI substrate.

To downscale the SiNW dimensions, electron beam (e-beam) lithography (EBL) is used for the SiNW device fabrication. Traditional photo-lithography is commonly used for device fabrication, but its resolution is limited by the wavelength of light source therefore it is difficult to define sub-100 nm structures in lab. The resolution of EBL, on the other hand, is limited by the spot size of e-beam, which can reach sub-10 nm [72]. Negative EBL resist hydrogen silsesquioxane (HSQ) with a high resolution of ~10 nm is selected to define the fine device structure.

To illustrate the top-down fabrication process, a process flow of an  $n^+p\text{-}n^+$  liquid-gate SiNWFET is presented in Figure 3.1 as an example. The SiNWFET was fabricated on a 100-mm SOI wafer. The SOI wafer comprised of a 55-nm-thick lightly  $p$ -type Si layer on top of a 145-nm-thick BOX layer. The top Si layer was thinned down from 55 nm to 30 nm by thermal oxidation and subsequent oxide etching using hydrofluoric acid (HF). An arsenic implantation was employed to form the heavily  $n$ -type ( $n^+$ ) S and D terminals while the channel region was protected by e-beam resist during the

implantation. The dopants in S/D regions were activated by rapid thermal processing (RTP) at 1000 °C for 10 s in N<sub>2</sub> atmosphere. Afterwards, the SiNWFET structure was defined with HSQ by EBL, followed by RIE of unprotected Si layer. To reduce the parasitic resistance and obtain ohmic contact, a 10-nm-thick nickel silicide (NiSi) layer was formed on the S/D pads with RTP at 400 °C for 30 s in N<sub>2</sub> atmosphere. A 5-nm-thick HfO<sub>2</sub> layer by atomic layer deposition (ALD) was deposited on the SiNW surface as a passivation layer. Before electrical measurements, forming gas annealing (FGA) was done at 400 °C for 30 min to passivate traps at the SiNW/oxide interface.

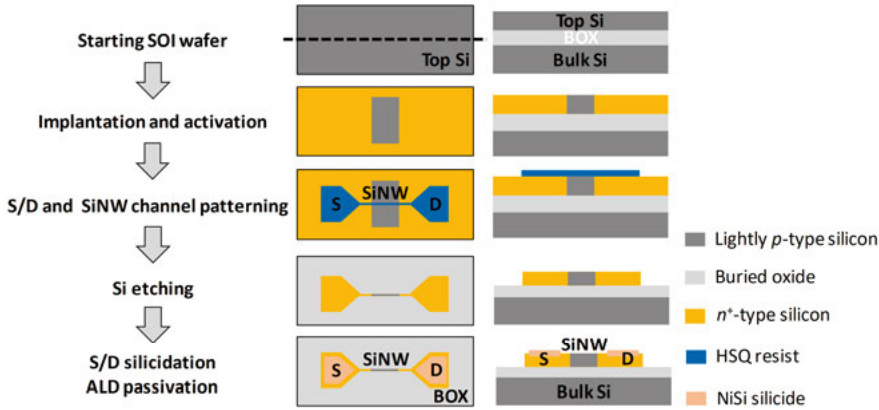
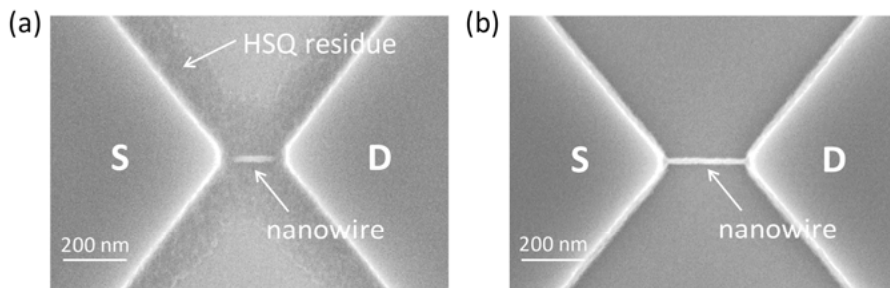


Figure 3.1. Fabrication process flow of an  $n^+ - p - n^+$  SiNWFET. Top-view and cross-sectional schematics of the device at each step are presented. The dashed curve annotates the position of cross-sectional cut.

The SiNW devices studied in this thesis are designed with different structures. Their fabrication processes are slightly modified from the base process described above. For example, the SiNWFETs for the single charge detection are designed without the gate oxide. Therefore, the ALD passivation process is skipped and instead an e-beam resist passivation layer is patterned on the S/D regions. For the SiNW resonators, SiNW vibration must be activated by an external force applied from a side gate, which is defined together with S/D terminals by EBL and RIE. The detailed fabrication processes of these devices can be found in the corresponding papers.

### 3.2 Process optimization

Some common challenges in the base fabrication process become greatly amplified for extremely downscaled SiNW devices. First, the proximity issue of EBL could damage the fine HSQ pattern [73]. In an ideal case, only HSQ in the designed pattern area is exposed by e-beam. However, the incident e-beam is scattered backwards in the substrate and expose the HSQ outside of the pattern to some extent. This issue is more severe for SiNW devices with smaller dimensions. The required dose of HSQ pattern for SiNW increases dramatically when the pattern width reaches the resolution of HSQ ( $\sim 10$  nm). Therefore, the backscattered e-beam becomes much stronger, which accumulates with that from S/D regions. If the overlapped dose of these backscattered e-beams gets close to the threshold value for HSQ reaction, some HSQ residue will be left between S/D regions, which may destroy the device structure (see Figure 3.2(a)).



*Figure 3.2. SEM images of HSQ pattern with (a) single-exposure and (b) double-exposure EBL processes.*

To solve the proximity issue, a double-exposure strategy is employed to optimize the HSQ pattern definition step. In the first exposure, only the NW pattern is exposed by e-beam. After development, the exposed HSQ pattern for the SiNW is left on the substrate, while the HSQ around the NW pattern is stripped by the developer. In the second exposure, a new HSQ layer is coated on the substrate and only the HSQ patterns for S/D regions are exposed. Although the strengths of the backscattered e-beams from SiNW and S/D regions are not weakened, their accumulation effect is eliminated and the fine device structure can be formed as designed (see Figure 3.2(b)).

The second issue is the RIE-induced roughness and associated defects on the SiNW surface [74]. According to Eq. (2.8), intrinsic noise of the SiNWFET increases with the shrunk dimensions, which inevitably limits its SNR. To address this noise issue, a  $H_2$  annealing process is explored. At elevated temperature, Si atoms on the SiNW surface will rearrange to reach the lower energy and this process is accelerated by  $H_2$  gas [75]. As shown in Figure 3.3, such rearrangement will smooth the SiNW surface and repair the

surface defects. Besides, the migration of Si atoms from the SiNW to S/D pads could further reduce the SiNW dimensions.

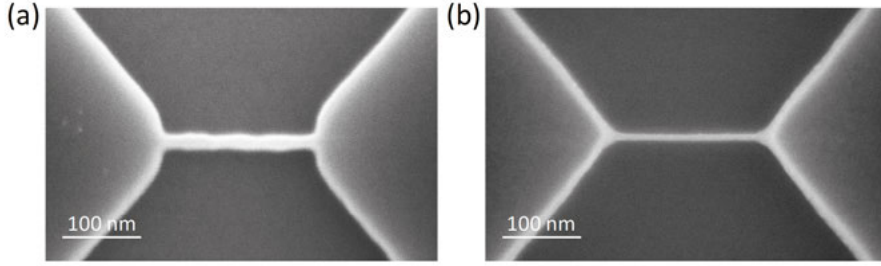


Figure 3.3. SEM images of SiNWs (a) without and (b) with  $H_2$  annealing.

### 3.3 Electrical characterization

Transfer characteristics and voltage noise of the liquid-gated SiNWFETs with and without the  $H_2$  annealing were measured in a 1 mM KCl solution. The results are plotted in Figure 3.4.  $V_G$  is applied to a Ag/AgCl reference electrode. The  $H_2$  annealing process indeed greatly improves the electrical performance of the SiNWFET, as evidenced by the near-ideal subthreshold slope  $SS \sim 60$  mV/dec (see Figure 3.4(a)). Moreover, the gate area normalized voltage noise ( $A \times S_{VG}$ ) is reduced by about one order of magnitude by the  $H_2$  annealing (see Figure 3.4(b)), which is comparable or even lower than that of some state-of-the-art SiNWFETs [70], [76]. The noise suppression by the  $H_2$  annealing process could improve the SNR and the detection limit of the SiNWFET sensor.

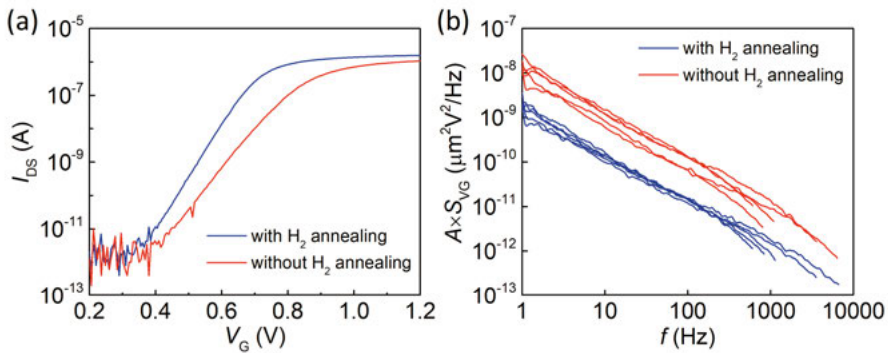


Figure 3.4. (a) Transfer characteristics and (b)  $A \times S_{VG}$  of the SiNWFETs with and without  $H_2$  annealing measured in 1 mM KCl at  $V_D = 100$  mV.  $S_{VG}$  was measured at  $I_{DS} = 1$  nA, 5 nA, 10 nA, 50 nA, and 100 nA.

## 4. Multiplexed Ion Detection Using SiNWFET Array

In recent years, multiplexed analyses of liquid samples have attracted great interest. The liquid samples may consist of multiple components, such as elemental ions, molecular ions, and small molecules. Such detection of liquid samples can provide rich information regarding water contaminations, one's physiological state, *etc.*

In this chapter, a SiNWFET sensor array is applied for multiplexed detection of sodium ion ( $\text{Na}^+$ ) and methylene blue ion ( $\text{MB}^+$ ). Mixed-matrix membrane (MMM) incorporated with the ion receptor, *i.e.*, ionophore, is used as the ion sensing layer, which is coated on the gate oxide surface of the SiNWFET. Multiplexed detection of  $\text{Na}^+$  and  $\text{MB}^+$  is demonstrated using  $\text{Na}^+$ - and  $\text{MB}^+$ -sensitive SiNWFET sensors integrated on one chip. However, the hydrophobic interaction between  $\text{MB}^+$  and polyvinyl chloride (PVC) matrix of the  $\text{Na}^+$ -MMM generates interference to  $\text{Na}^+$  sensing and limits the multiplexed detection range. A hydrophilic additive, *i.e.*, polyethylene glycol (PEG), is doped into the  $\text{Na}^+$ -MMM, which is proven to suppress the hydrophobic interaction with  $\text{MB}^+$  and therefore expands the multiplexed detection range.

### 4.1 Working principle of MMM

The MMM is based on PVC matrix and contains ionic site (KTpCIPB) and specific ionophore for the target ion. Ionophore for elemental ion is commercially available. Na-ionophore III is used for  $\text{Na}^+$  sensing, because its cavity fits well with  $\text{Na}^+$  in size. Since the size of  $\text{MB}^+$  is much larger than elemental ions, commercial ionophores with a high binding affinity to  $\text{MB}^+$  are currently not available. A new class of synthetic receptors, *i.e.*, metal-organic supercontainer (MOSC), is proven to be an efficient host system for such large molecular ions [77]. The synthesized MOSC, designated as **1-Co**, is used as the ionophore for  $\text{MB}^+$ . The MMM components are solved in Tetrahydrofuran (THF), and the MMM solution is drop-casted on the gate oxide surface of SiNWFET for functionalization. Prior to sensing

measurements, the  $\text{Na}^+$ -MMM is conditioned in a 100 mM NaCl solution for 4 h and  $\text{MB}^+$ -MMM is conditioned in a 10  $\mu\text{M}$  MB solution for 10 h.

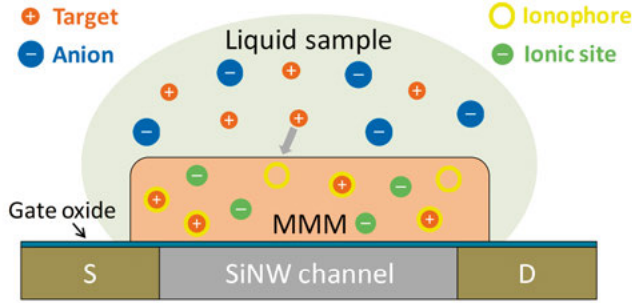


Figure 4.1. Schematic of MMM-functionalized SiNWFET.

Schematic of the MMM-functionalized SiNWFET is presented in Figure 4.1. In the conditioning process, target ions, *i.e.*,  $\text{Na}^+$  and  $\text{MB}^+$ , are captured into the MMM from liquid sample due to the strong affinity of the ionophores through an ion-exchange process with counter ion of the ionic site ( $\text{K}^+$ ). When the ionophore molecules incorporated in MMM are more than ionic sites stoichiometrically, the number of target ions in the MMM is approximately fixed by that of the ionic sites. Therefore, phase boundary potential ( $E_{\text{PB}}$ ) at the MMM/liquid interface depends on the target ion concentration in the liquid sample ( $c_{\text{liq}}$ ) [78]:

$$E_{\text{PB}} = E_{\text{PB}}^0 + 2.3 \frac{kT}{q} \log_{10} c_{\text{liq}}, \quad (4.1)$$

where  $E_{\text{PB}}^0$  is the phase boundary potential constant. When  $c_{\text{liq}}$  is increased, more cations ( $\text{Na}^+$  or  $\text{MB}^+$ ) accumulates on the MMM side of MMM/liquid interface. To maintain the charge neutrality, equal number of anion ( $\text{Cl}^-$ ) will accumulate on the liquid side. Consequently, a larger electrical field and a higher phase boundary potential are produced at the MMM/liquid interface. When the electrical potential of the liquid sample is fixed by a RE, the observed  $\Delta V_{\text{T}}$  of the SiNWFET equals  $\Delta E_{\text{PB}}$ . Consequently, variation of  $c_{\text{liq}}$  in liquid sample will change  $V_{\text{T}}$  of the SiNWFET by 59.2mV/dec according to Eq. (4.1).

## 4.2 Multiplexed detection of molecular and elemental ions

Prior to multiplexed detection, the SiNWFET sensors were selectively functionalized with MB<sup>+</sup>- and Na<sup>+</sup>-MMMs. The MB<sup>+</sup> detection was conducted by measuring  $\Delta V_T$  of MB<sup>+</sup>-sensitive SiNWFET with the MB<sup>+</sup> concentration ( $c_{MB}$ ) increasing from 10 nM to 1 mM. The background solution used for the measurement contained 1 mM KCl. The results are shown in Figure 4.2(a). As  $c_{MB}$  increases, the surface of MB<sup>+</sup>-MMM becomes more positively charged, leading to a negative shift of  $V_T$ . The MB<sup>+</sup>-sensor shows a near-Nernstian response up to  $c_{MB} = 30 \mu\text{M}$ . The response of  $V_T$  starts to deviate from the ideal trend when  $c_{MB}$  is above 100  $\mu\text{M}$ . Such deviation can be ascribed to the co-extraction of MB<sup>+</sup> and its counter ion (Cl<sup>-</sup>) from the liquid into the MMM, which is called Donnan failure [79]. A lower detection limit of  $\sim 1 \mu\text{M}$  is extrapolated from the MB<sup>+</sup> response curve in Figure 4.2(a).

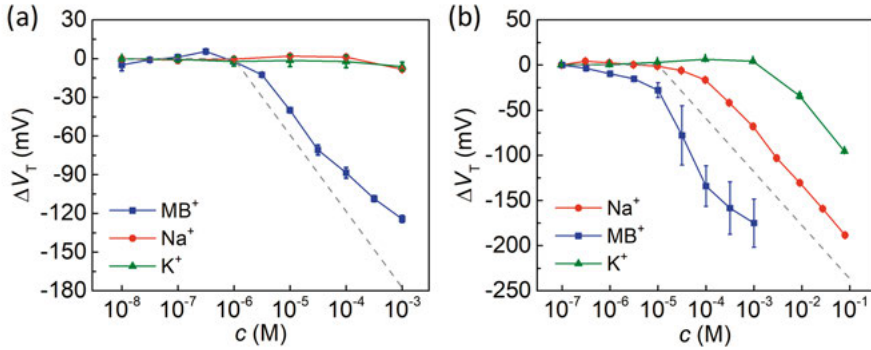


Figure 4.2. Potential responses of (a) MB<sup>+</sup>-MMM and (b) Na<sup>+</sup>-MMM functionalized SiNWFETs to the target and interfering ions. The dashed lines indicate the Nernstian responses.

The selectivity of MB<sup>+</sup>-sensor was also investigated by measuring its response to the common elemental ions, *i.e.*, Na<sup>+</sup> and K<sup>+</sup>, which are widely present in aqueous samples. Figure 4.2(a) indicates the negligible responses of MB<sup>+</sup>-sensor to Na<sup>+</sup> and K<sup>+</sup> with their concentrations  $c_{Na}$  and  $c_K$  up to 1 mM. This is because these elemental ions are too small to fit into the cavity of MB<sup>+</sup> MOSC. The superior selectivity against elemental ions is a clear advantage of MOSCs in the recognition and detection of molecular ions. These results demonstrate the high sensitivity and selectivity of the MB<sup>+</sup>-sensor and the successful functionalization using ionophore doped MMM.

Na<sup>+</sup>-sensor was characterized by measuring its potential responses to target ion Na<sup>+</sup> and interfering ions K<sup>+</sup> and MB<sup>+</sup> in a similar way. As shown in Figure 4.2(b), the Na<sup>+</sup>-sensor exhibits a near-Nernstian response to  $c_{Na}$  in a wide range from 100  $\mu\text{M}$  to 100 mM with a lower detection limit of  $\sim 60 \mu\text{M}$ .



Meanwhile, the  $\text{Na}^+$ -sensor shows large responses towards  $\text{K}^+$  and  $\text{MB}^+$  once  $c_{\text{K}}$  and  $c_{\text{MB}}$  are above a certain threshold, *i.e.*,  $\sim 1$  mM for  $\text{K}^+$  and  $\sim 10$   $\mu\text{M}$  for  $\text{MB}^+$ . The response of  $\text{Na}^+$ -sensor to  $\text{K}^+$  can be ascribed to the fact that  $\text{K}^+$  has a similar size with  $\text{Na}^+$ , and the size selectivity of  $\text{Na}^+$ -ionophore to  $\text{K}^+$  is poor [80]. The response of  $\text{Na}^+$ -sensor to  $\text{MB}^+$  can be explained by the hydrophobic interaction between  $\text{MB}^+$  and PVC matrix of the  $\text{Na}^+$ -MMM. Hydrophobic  $\text{MB}^+$  could partition into the PVC matrix during the measurements and generate interference to the  $\text{Na}^+$  sensing. This is described in more detail in **Paper I**. This partitioning process and the interference are under poor control, as indicated by the large variations of  $\Delta V_{\text{T}}$  among different measurements. Therefore, for multiplexed detection of  $\text{Na}^+$  and  $\text{MB}^+$ , it is crucial to keep  $c_{\text{MB}}$  below the threshold value, *i.e.*,  $\sim 10$   $\mu\text{M}$ , to avoid the non-specific interference from  $\text{MB}^+$ .

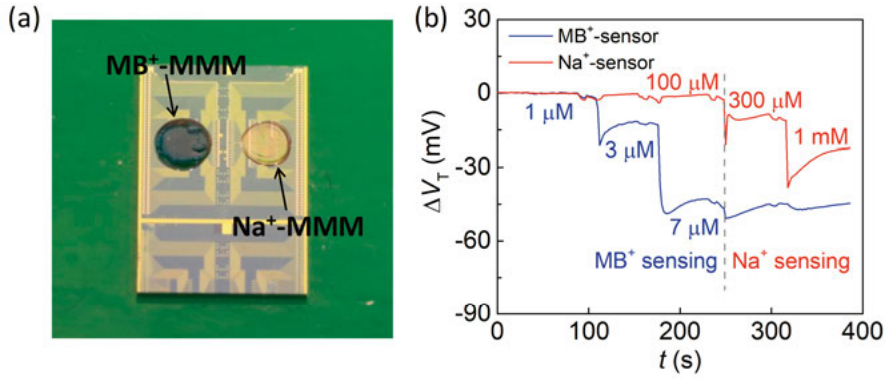


Figure 4.3. (a) Optical image of a SiNWFEF chip with  $\text{MB}^+$ - and  $\text{Na}^+$ -sensors. (b) Multiplexed detection of  $\text{MB}^+$  and  $\text{Na}^+$ .

To conduct multiplexed detection,  $\text{MB}^+$ - and  $\text{Na}^+$ -sensors were integrated on one chip as seen in Figure 4.3(a). During the multiplexed detection,  $c_{\text{MB}}$  in the liquid sample is kept below the threshold, *i.e.*, 10  $\mu\text{M}$ . As shown in Figure 4.3(b), the initial  $c_{\text{MB}}$  and  $c_{\text{Na}}$  are 1 and 100  $\mu\text{M}$ , respectively. First,  $c_{\text{MB}}$  is increased from 1 to 3  $\mu\text{M}$  and then from 3 to 7  $\mu\text{M}$ , the corresponding  $\Delta V_{\text{T}}$  of  $\text{MB}^+$ -sensor are -12.5 and -30.7 mV, respectively. Meanwhile, the  $\text{Na}^+$ -sensor shows negligible responses. Afterwards,  $c_{\text{Na}}$  is increased from 100 to 300  $\mu\text{M}$  and then from 300  $\mu\text{M}$  to 1 mM, the corresponding  $\Delta V_{\text{T}}$  of  $\text{Na}^+$ -sensor is -9.4 and -13.0 mV. Also, negligible responses are observed for the  $\text{MB}^+$ -sensor. This multiplexed detection is demonstrated in a narrow range, because  $c_{\text{MB}}$  must be kept below the threshold to avoid the interference of  $\text{MB}^+$  to  $\text{Na}^+$ -sensor. A solution of such problem is presented in Chapter 4.3.

### 4.3 PEG doping for improving ion selectivity

Hydrophobic ions in a complex liquid sample can generate considerable interference to membrane based ion-sensitive sensors. The interference is understood due to the partitioning of the hydrophobic ions into the polymer membrane matrix. In this chapter, we demonstrate that, by incorporating hydrophilic PEG into the membrane matrix [81], [82], such partitioning can be significantly suppressed and thus the selectivity of membrane based sensors to hydrophobic ions is greatly improved.

Target ion can be specifically captured by the ionophore in MMM. However, hydrophobic interfering ions can also partition into MMM due to the hydrophobic nature of MMM matrix. In the presence of both target and interfering ions, *i.e.*,  $\text{Na}^+$  and  $\text{MB}^+$  respectively,  $E_{\text{PB}}$  at the MMM/liquid interface can be expressed with a semi-empirical form [78]:

$$E_{\text{PB}} = E_{\text{PB}}^0 + 2.3 \frac{kT}{q} \log_{10} (c_{\text{Na}} + K_{\text{Na,MB}} c_{\text{MB}}), \quad (4.2)$$

where  $K_{\text{Na,MB}}$  is the selectivity coefficient of  $\text{Na}^+$ -MMM against  $\text{MB}^+$ .  $K_{\text{Na,MB}}$  reflects affinity of the  $\text{Na}^+$ -MMM towards  $\text{Na}^+$  and  $\text{MB}^+$ . A smaller value of  $K_{\text{Na,MB}}$  indicates that the  $\text{Na}^+$ -MMM has a lower affinity to  $\text{MB}^+$  and is less vulnerable to the interference from  $\text{MB}^+$ .

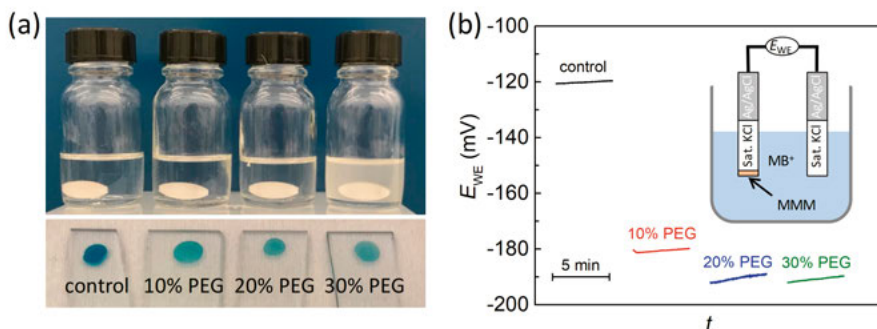


Figure 4.4. (a) Optical images of  $\text{Na}^+$ -MMM THF solutions with different PEG concentrations (upper) and  $\text{Na}^+$ -MMMs on glass after conditioning in a  $100 \mu\text{M}$   $\text{MB}^+$  solution for 10 min (lower). (b)  $E_{\text{WE}}$  of ISEs fabricated with different  $\text{Na}^+$ -MMMs measured in a  $10 \mu\text{M}$   $\text{MB}^+$  solution for 5 min. Inset: schematic of  $E_{\text{WE}}$  measurement setup.

To demonstrate the advantages of PEG doping, four types of  $\text{Na}^+$ -MMMs were prepared: Na-ionophore incorporated MMM without PEG ( $\text{Na}^+$ -MMM-control), and with 10%, 20%, and 30% PEG (weight ratio to PVC matrix) ( $\text{Na}^+$ -MMM-10%,  $\text{Na}^+$ -MMM-20%, and  $\text{Na}^+$ -MMM-30%, respectively). As

shown in Figure 4.4(a) (upper), the THF solutions of Na<sup>+</sup>-MMM-control, Na<sup>+</sup>-MMM-10%, and Na<sup>+</sup>-MMM-20% are transparent, while that of Na<sup>+</sup>-MMM-30% is turbid with visible particles since the excessive PEG are not dissolved. The different Na<sup>+</sup>-MMMs were immersed in 100  $\mu$ M MB<sup>+</sup> for 10 min to test partitioning of MB<sup>+</sup> into the Na<sup>+</sup>-MMMs. As shown in Figure 4.4(a) (lower), all of the PEG-doped Na<sup>+</sup>-MMMs present a light blue color in comparison to the dark blue color of Na<sup>+</sup>-MMM-control. Evidently, hydrophilic PEG can reduce hydrophobicity of the Na<sup>+</sup>-MMMs, and therefore lower their affinity to hydrophobic MB<sup>+</sup> and impede the partitioning of MB<sup>+</sup>.

The effect of PEG doping on MB<sup>+</sup> partitioning was further examined by measuring working electrode potential ( $E_{WE}$ ) of ISEs produced with the four Na<sup>+</sup>-MMMs. To fabricate these ISEs, pipette tips were dipped into the MMM solutions, allowing  $\sim 10$   $\mu$ L solution to fill the pipette tips by capillary force. Then, Ag/AgCl pellets were inserted into the pipette body. Saturated KCl solution was injected into the pipette body to complete ISE fabrication. The ISE has a symmetric configuration with Ag/AgCl reference electrode as seen in the inset of Figure 4.4(b). Therefore, the contribution from standard chemical potential of the MMM is canceled out and  $E_{WE}$  only depends on the ratio of  $c_{MB}$  in the liquid sample to that in the MMM. As a result,  $E_{WE}$  can quantitatively indicate the amount of MB<sup>+</sup> partitioning into the MMM [83]. As shown in Figure 4.4(b),  $E_{WE}$  becomes more negative with the increase of PEG concentration in the Na<sup>+</sup>-MMMs measured in a 10  $\mu$ M MB<sup>+</sup> solution. For Na<sup>+</sup>-MMM-10%,  $E_{WE}$  is lowered by  $\sim 60$  mV in comparison to that of Na<sup>+</sup>-MMM-control, which can be converted to  $\sim 10$  times reduction of  $c_{MB}$  in the MMM. Further increase of PEG concentration beyond 10% shows less effect on  $E_{WE}$ , which is consistent with the observed color differences of the Na<sup>+</sup>-MMMs shown in Figure 4.4(a) (lower).

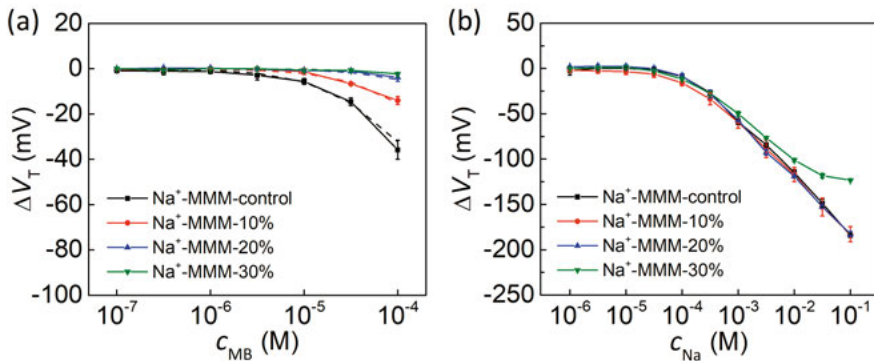


Figure 4.5.  $\Delta V_T$  as a function of (a)  $c_{MB}$  in 1 mM NaCl and (b)  $c_{Na}$  in 1 mM KCl of Na<sup>+</sup>-sensors functionalized with different Na<sup>+</sup>-MMMs. In (a), the solid and dashed curves represent measured and fitting results, respectively.

SiNWFETs were functionalized with the four Na<sup>+</sup>-MMMs, and their potential responses to MB<sup>+</sup> were measured to characterize the selectivity against MB<sup>+</sup>. The measurements were conducted with a background solution of 1 mM NaCl to keep a constant ionic strength. Figure 4.5(a) presents  $\Delta V_T$  of these SiNWFETs versus  $c_{MB}$ . The SiNWFET with higher PEG doped MMM shows a lower response to MB<sup>+</sup>. The selectivity coefficients  $K_{Na, MB}$  of different Na<sup>+</sup>-MMMs are extracted by fitting the response curves with Eq. (4.2). The fitting results are shown as the dashed curves in Figure 4.5(a) and the extracted  $K_{Na, MB}$  is listed in Table 4.1. Evidently, PEG doping improves the selectivity of the Na<sup>+</sup>-MMM against the hydrophobic molecular ion, *i.e.*, MB<sup>+</sup>, which is indicated by the reduced  $K_{Na, MB}$ . In particular,  $K_{Na, MB}$  of Na<sup>+</sup>-MMM-20% and Na<sup>+</sup>-MMM-30% is reduced by more than one order of magnitude in comparison to that of Na<sup>+</sup>-MMM-control.

Table 4.1. Extracted  $K_{Na, MB}$  of different Na<sup>+</sup>-MMMs.

MMM	Na <sup>+</sup> -MMM-control	Na <sup>+</sup> -MMM-10%	Na <sup>+</sup> -MMM-20%	Na <sup>+</sup> -MMM-30%
$K_{Na, MB}$	25	8	2	0.9

Possible adverse effects of PEG doping were evaluated by conducting Na<sup>+</sup> sensing with the control and PEG-doped Na<sup>+</sup>-MMMs. The Na<sup>+</sup> sensing measurement results are plotted in Figure 4.5(b). The responses to  $c_{Na}$  of Na<sup>+</sup>-MMM-control, Na<sup>+</sup>-MMM-10%, and Na<sup>+</sup>-MMM-20% basically overlap, demonstrating that PEG doping has no significant adverse effects on Na<sup>+</sup> sensing when PEG concentration is below 20%. However, the response of Na<sup>+</sup>-MMM-30% deviates significantly when  $c_{Na}$  is above 10 mM, which indicates that further increase of PEG doping in Na<sup>+</sup>-MMM may lead to deterioration of Na<sup>+</sup> sensitivity, particularly when  $c_{Na}$  is high. Such deviation might arise from the co-extraction of Na<sup>+</sup> and Cl<sup>-</sup> from the liquid sample into the MMM [79]. The co-extraction process is likely enhanced in Na<sup>+</sup>-MMM-30%, since the reduced hydrophobicity might facilitate the extraction of Cl<sup>-</sup> into the MMM.

Since Na<sup>+</sup>-MMM-20% shows the improved selectivity against MB<sup>+</sup> and negligible adverse effects in Na<sup>+</sup> sensing, it is selected to expand the multiplexed detection range for MB<sup>+</sup> and Na<sup>+</sup> ions. As shown in Figure 4.6, the initial concentrations of MB<sup>+</sup> and Na<sup>+</sup> are 1 and 100  $\mu$ M, respectively.  $c_{MB}$  in the liquid sample is first increased from 1 to 10  $\mu$ M and then from 10 to 100  $\mu$ M while  $c_{Na}$  is maintained at 100  $\mu$ M. Correspondingly, the MB<sup>+</sup>-sensor shows  $-65.3$  and  $-52.3$  mV of  $\Delta V_T$ , respectively, while the responses of the Na<sup>+</sup>-sensor are negligible. Then,  $c_{Na}$  is increased from 100 to 300  $\mu$ M and then from 300  $\mu$ M to 1 mM, and  $c_{MB}$  is maintained at 100  $\mu$ M. The corresponding values of  $\Delta V_T$  of Na<sup>+</sup>-sensor are  $-22.7$  and  $-30.5$  mV,

respectively, while  $V_T$  of the  $\text{MB}^+$ -sensor remains unaltered. In Chapter 4.2, the multiplexed detection is performed with  $c_{\text{MB}}$  only up to  $7\ \mu\text{M}$ , above which hydrophobic  $\text{MB}^+$  will generate large interference to the  $\text{Na}^+$ -sensor. PEG doping into the  $\text{Na}^+$ -MMM clearly suppresses such interference and greatly improves the tolerance of the  $\text{Na}^+$ -sensor to  $\text{MB}^+$ . Consequently, multiplexed detection is performed in a much wider  $c_{\text{MB}}$  range, *i.e.*, from 1 to  $100\ \mu\text{M}$ . It should be noted that the demonstrated PEG doping strategy for membrane based ion sensors will not be limited to the particular ions studied in this work. It can be generally applicable for other membrane based sensors.

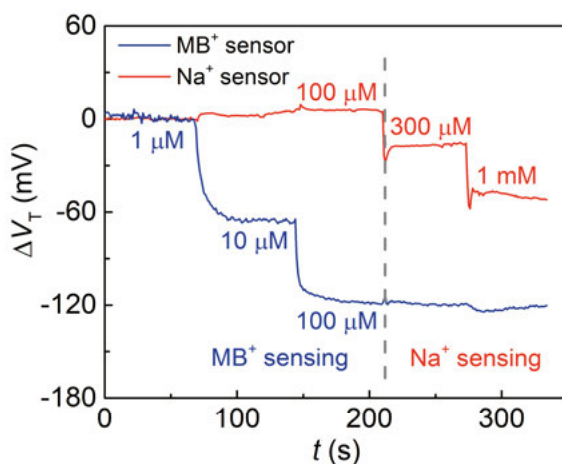


Figure 4.6. Multiplexed detection of  $\text{MB}^+$  and  $\text{Na}^+$ . The  $\text{Na}^+$ -sensor is functionalized with  $\text{Na}^+$ -MMM-20%.

## 5. Single Charge Detection in Liquid Using Sub-10 nm SiNWFETs

As discussed in Chapter 2.1, three technical prerequisites must be satisfied to achieve single charge detection in liquid sample using a SiNWFET. First, dimensions of the SiNW need to be extremely downscaled for an enhanced charge sensitivity. Second, intrinsic device noise of the SiNWFET should be low to achieve a high SNR. Third, the SiNW surface should have a single activated receptor to prevent ensemble signals.

In this chapter, these three prerequisites are carefully addressed and the events of a single  $H^+$  interacting with a sensing surface are successfully observed using sub-10 nm SiNWFETs. The SiNW surface is smoothed by a  $H_2$  annealing process to suppress the intrinsic device noise and further shrink the SiNW width and height to sub-10 nm. The SiNWFETs are gate oxide free, and surface Si dangling bonds (DBs) are employed as the receptors to capture/emit  $H^+$  ions in liquid sample. Since the majority of DBs are passivated with covalent H-terminations using a wet etching process in buffered HF, the remaining DBs can be activated individually as a single  $H^+$  receptor. The single  $H^+$ -DB interaction produces the  $I_{DS}$  switching signals between two discrete levels. Such switching can be ascribed to the change of local Coulomb scattering strength and therefore electron mobility. The kinetics of single  $H^+$ -DB interaction and its correlation to energy barriers at the SiNW/electrolyte interface are systematically investigated.

### 5.1 Direct observation of single $H^+$ -DB interaction

To realize the direct detection of single  $H^+$ -DB interaction,  $n^+-p-n^+$  type SiNWFETs without gate oxide layer were fabricated on (100) SOI substrate with an optimized CMOS-compatible process. As shown in Figure 5.1(a), S/D regions of the SiNWFET are heavily  $n$ -doped, while the SiNW consists of a 150-nm-long lightly  $p$ -type region (gray) in the center and 50-nm-long heavily  $n$ -type regions (yellow) on both ends. The width and height of the SiNW were shrunk to sub-10 nm by the  $H_2$  annealing process, during which the RIE-induced surface defects on the SiNW surface were also eliminated. A cross-sectional transmission electron microscope (XTEM) image of the SiNW

channel after  $H_2$  annealing is shown in Figure 5.1(b). The channel width and height measured from the image are 7 and 9 nm, respectively.

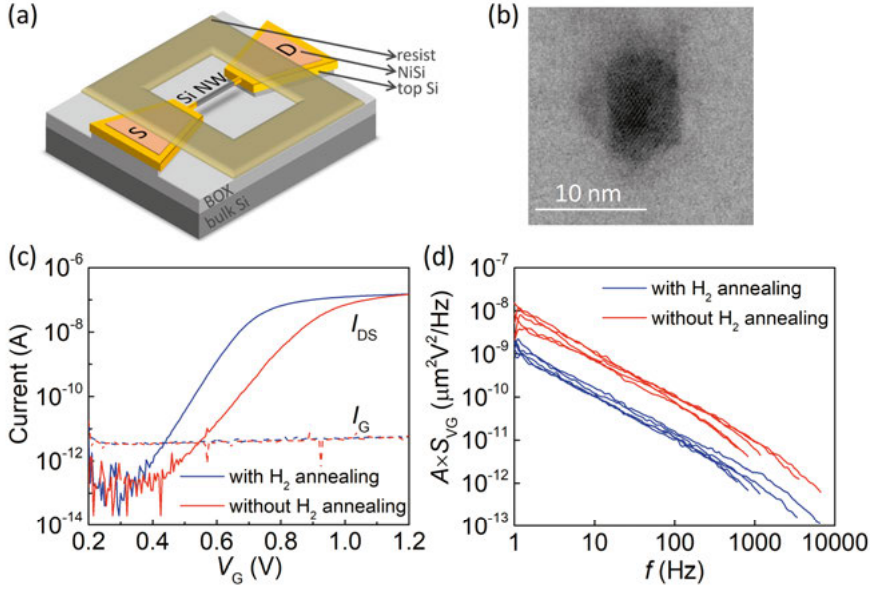


Figure 5.1. (a) Three-dimensional schematic of the gate oxide free SiNWFET. (b) XTEM image of the SiNW with  $H_2$  annealing. (c) Transfer characteristics of the SiNWFETs with and without  $H_2$  annealing measured in 1 mM KCl at  $V_D = 10$  mV. (d)  $A \times S_{VG}$  of the SiNWFETs with and without  $H_2$  annealing measured in 1 mM KCl at  $V_D = 10$  mV.  $S_{VG}$  was measured at  $I_{DS} = 1$  nA, 5 nA, 10 nA, 50 nA, and 100 nA.

Without the gate oxide layer, modulation of the SiNW channel conductance by the single  $H^+$ -DB interaction can be enhanced, as the distance where the interaction takes place to the SiNW channel is minimized. To avoid excessive leakage current in liquid, the S/D pads and leads were passivated by an e-beam resist layer while the SiNW channel was exposed to liquid sample for  $H^+$  detection. Typical transfer characteristics of the SiNWFETs with and without  $H_2$  annealing are shown in Figure 5.1(c). Gate leakage currents ( $I_G$ ) are negligible and  $I_{DS}$  can be modulated by 5 orders of magnitude, which indicates that the EDL works as a good gate dielectric. As discussed in Chapter 3.2,  $H_2$  annealing can improve the SS and suppress the intrinsic noise of the SiNWFET (see Figure 5.1(c) and (d)).

On the SiNW surface, the non-saturated valence electrons form Si DBs with a density of  $\sim 10^{14} \text{ cm}^{-2} \cdot \text{eV}^{-1}$ . The DBs can act as the receptors of  $H^+$  in liquid sample. Considering dimensions of the SiNW channel, the total number of DBs is  $\sim 3000$ , which is too high to detect single  $H^+$  capture/emission events. It is known that most of Si DBs can be passivated by a wet chemical process

in buffered HF with covalent H-terminations. After the passivation, the DB density is reduced to  $\sim 10^{10} \text{ cm}^{-2} \cdot \text{eV}^{-1}$  [84], [85]. With such low density, the number of DBs on the SiNW channel surface is estimated to be 0.3 per SiNW, which suggests a high probability of a single DB activated as  $\text{H}^+$  receptor on the tiny SiNW channel surface.

Detection of the single  $\text{H}^+$ -DB interaction was performed in a 10 mM HCl solution with a constant gate overdrive, *i.e.*,  $V_G - V_T = 129.4 \text{ mV}$ .  $I_{\text{DS}}$  was monitored in real-time with a sampling frequency of 3 kHz. A typical  $I_{\text{DS}}$  trace is depicted in Figure 5.2(a) (upper), showing  $I_{\text{DS}}$  switching between two levels with  $\Delta I_{\text{DS}} \sim 3 \text{ nA}$ . For small MOSFETs, capture and emission of a carrier by a trap near Si/oxide interface could also result in a similar  $I_{\text{DS}}$  switching, leading to so-called random telegraph noise (RTN) [86]. To verify if the observed two-level  $I_{\text{DS}}$  switching correlates to the carrier trapping/detrapping processes occurring near the interface between SiNW and native oxide, a control experiment was conducted on the same SiNWFET but in deionized (DI) water.  $I_{\text{DS}}$  for measurement in DI water was intentionally kept the same as that in 10 mM HCl to ensure that the SiNW channel was biased to the same condition in both cases. As indicated in Figure 5.2(a) (middle), the  $I_{\text{DS}}$  trace measured in DI water does not show the two-level switching. This result confirms that the two-level  $I_{\text{DS}}$  switching observed in 10 mM HCl is not generated inside the SiNWFET device, otherwise it should also appear when measured in DI water since the device is biased to the same condition in both cases. To exam if  $\text{Cl}^-$  contributes to the  $I_{\text{DS}}$  switching, another control experiment was conducted in a 10 mM KCl solution. As shown in Figure 5.2(a) (lower),  $I_{\text{DS}}$  switching is not observed in 10 mM KCl. This confirms that the  $I_{\text{DS}}$  switching in 10 mM HCl is generated by the interaction between  $\text{H}^+$  (not  $\text{Cl}^-$ ) and the DB.

Figure 5.2(b) presents a schematic view of the interface between SiNW and HCl solution. There are three different terminations on the SiNW surface: single Si DB, covalent Si-H terminations, and Si-O $^-$  terminations on discrete native oxide islands. The EDL on the electrolyte side is formed by a Stern layer and a diffuse layer [57]. The capacitances of Stern layer ( $C_{\text{st}}$ ) and diffuse layer ( $C_{\text{dif}}$ ) are connected in series with the SiNW capacitance ( $C_{\text{Si}}$ ). The electrical potential distribution across the SiNW/HCl interface is illustrated at the bottom of Figure 5.2(b). The single DB can capture and emit one  $\text{H}^+$  ion at the Stern/diffuse layer interface, which is the closest plane that  $\text{H}^+$  ions can reach towards the SiNW surface. When emitted from the DB to the electrolyte, the  $\text{H}^+$  ion must overcome the electrical potential barrier across Stern layer ( $V_{\text{st}}$ ). The -OH group on the SiNW surface, which has a much lower effective density than that on an oxide surface, can also interact with  $\text{H}^+$  ions but gives a weak buffer capacity and thus a weak *pH* response. Detailed discussion of the -OH group density can be found in **Paper III**.



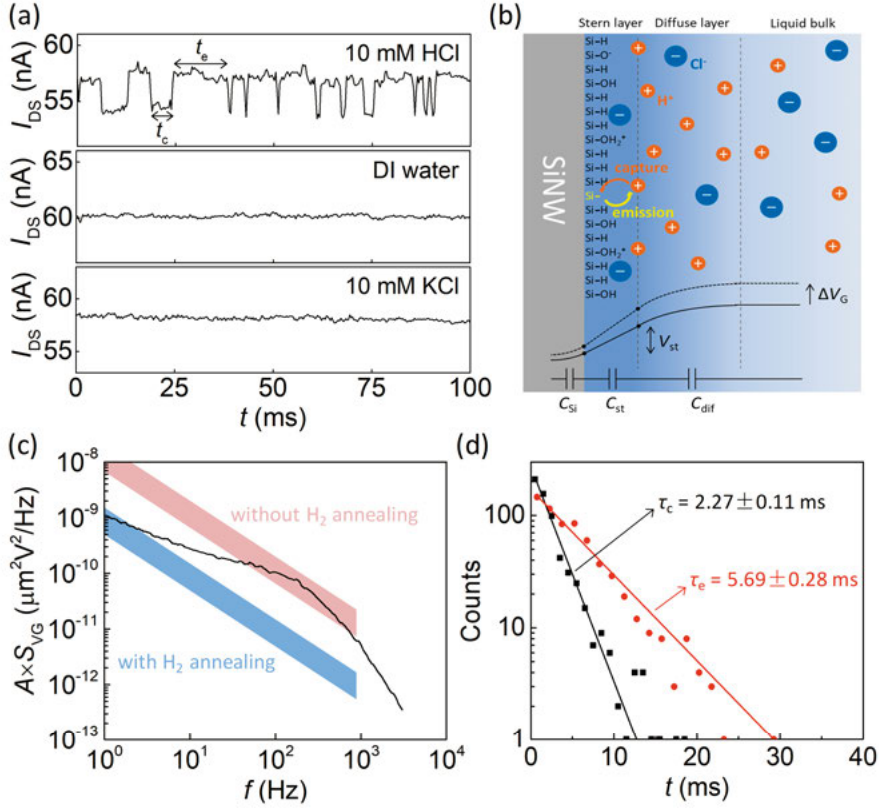


Figure 5.2. (a)  $I_{DS}$  sampling results in 10 mM HCl, DI water, and 10 mM KCl. The sampling frequency is 3 kHz. (b) Schematic of the SiNW/HCl interface. The single DB captures and emits a  $H^+$  ion from/to the Stern/diffuse layer interface. The total potential drop is shared by the capacitances of SiNW, Stern layer, and diffuse layer. (c)  $A \times S_{VG}$  (black curve) generated by the single  $H^+$ -DB interaction measured in 10 mM HCl. The intrinsic noise of the SiNWFET with  $H_2$  annealing (blue band) is much lower than the signal, while that of the SiNWFET without  $H_2$  annealing (red band) overwhelms the signal. (d) Statistical analysis of capture and emission times of the single  $H^+$ -DB interaction. They are in good agreement with Poisson distribution. The time constants  $\tau_c$  and  $\tau_e$  are extracted from the fitted slopes.

The  $H^+$  receptor, DB, on the SiNW channel surface is an acceptor-type electron trap [87]. The DB is saturated with an electron from the channel, since our SiNWFET is biased to strong inversion during the sensing experiments. The DB becomes negatively charged when filled with the electron, and enhances local Coulomb scattering in the SiNW channel. The negatively charged DB could further capture a  $H^+$  ion from the electrolyte and become neutralized. This would reduce the local Coulomb scattering strength and thus

increase  $I_{\text{DS}}$ . The time when  $I_{\text{DS}}$  remains at the low-state is the capture time  $t_c$  and the time at the high-state is the emission time  $t_e$  (see Figure 5.2(a)).

The  $I_{\text{DS}}$  switching measured in 10 mM HCl is further analyzed in frequency domain and its PSD is plotted in Figure 5.2(c), which shows a Lorentzian-shape profile with a corner frequency of  $\sim 150$  Hz. To illustrate the beneficial effect gained with  $\text{H}_2$  annealing, the intrinsic device noises of the SiNWFETs with and without  $\text{H}_2$  annealing are also included in the same PSD plot as references. The Lorentzian hump of the single  $\text{H}^+$ -DB interaction is completely shadowed by the  $1/f$  spectrum of the SiNWFET without  $\text{H}_2$  annealing (red band), which indicates that the capture/emission events of a single  $\text{H}^+$  cannot be resolved on the SiNWFET without  $\text{H}_2$  annealing. Distributions of  $t_c$  (black rectangles) and  $t_e$  (red circles) extracted from the  $I_{\text{DS}}$  trace are presented in Figure 5.2(d), which are in excellent agreement with Poisson statistics, *i.e.*, the count is proportional to  $\exp(t/\tau)$  [88]. The time constants  $\tau_c$  and  $\tau_e$  can be extracted from the fitted slopes, *i.e.*,  $\tau_c = 2.27$  ms and  $\tau_e = 5.69$  ms.

## 5.2 Single $\text{H}^+$ -DB interaction analysis

The  $I_{\text{DS}}$  traces of the SiNWFET with  $\text{H}_2$  annealing (referred as Dev. A) recorded at different  $V_G - V_T$  in 10 mM HCl are plotted in Figure 5.3(a). The histograms of three representative  $I_{\text{DS}}$  traces are also presented in Figure 5.3(b), and each trace shows two discrete Gaussian peaks [89]. As discussed before, the current peaks of low- and high-states correspond to the empty and filled states of the DB, respectively. At  $V_G - V_T = 79.5$  mV, the lower peak is dominating, which indicates that the DB is mostly empty. As  $V_G$  increases, the lower peak gradually decreases while the higher peak increases and finally becomes dominant, indicating that the DB is mostly filled with  $\text{H}^+$ . To quantitatively represent the DB states, occupation probability ( $P$ ) is calculated by the ratio of the areas of the lower and higher Gaussian peaks. The transition from the empty to the filled DB is clearly illustrated by the increased  $P$  at higher  $V_G$  (see Figure 5.3(c)). As illustrated in Figure 5.2(b), Stern layer shares a larger potential drop  $V_{\text{st}}$  with the increased  $V_G$ . Therefore the energy of  $\text{H}^+$  bound by the DB is lowered comparing to that at Stern/diffuse layer interface. Consequently, the DB has a higher probability to be filled with the  $\text{H}^+$  from the Stern/diffuse layer interface at a higher  $V_G$ .

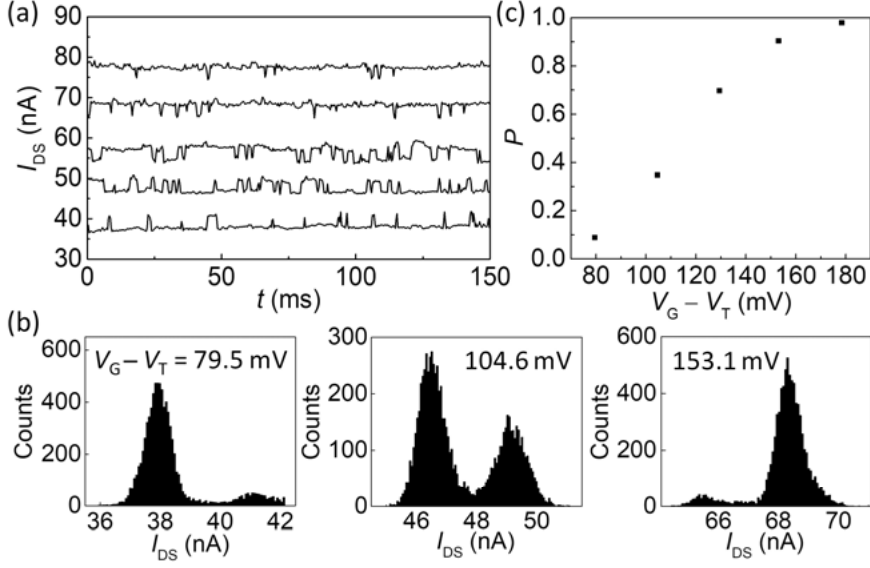


Figure 5.3. (a)  $I_{DS}$  sampling results at varied  $V_G - V_T$  in 10 mM HCl with a 3 kHz sampling frequency. (b) Three representative histograms of  $I_{DS}$ . (c) Occupation probability of the DB as a function of  $V_G - V_T$ .

The time constants  $\tau_c$  and  $\tau_e$  extracted from the  $I_{DS}$  traces at different  $V_G - V_T$  are plotted in Figure 5.4(a).  $\tau_c$  decreases with the increased  $V_G$  while  $\tau_e$  shows an opposite trend. As illustrated by the dashed line of potential distribution at the bottom of Figure 5.2(b), the voltage drops across diffuse layer and Stern layer are enlarged as  $V_G$  increases. According to Boltzmann distribution, the increased potential drop across the diffuse layer will lead to an increased  $H^+$  concentration at the Stern/diffuse layer interface ( $c_{Hs}$ ). As a result, it becomes easier for the DB to capture a  $H^+$  ion from the Stern/diffuse layer interface, thus resulting in a shorter  $\tau_c$ . Meanwhile, the emission of a  $H^+$  ion from the DB becomes more difficult due to the higher potential barrier across the Stern layer. Therefore, a larger  $\tau_e$  is observed with increasing  $V_G$ .

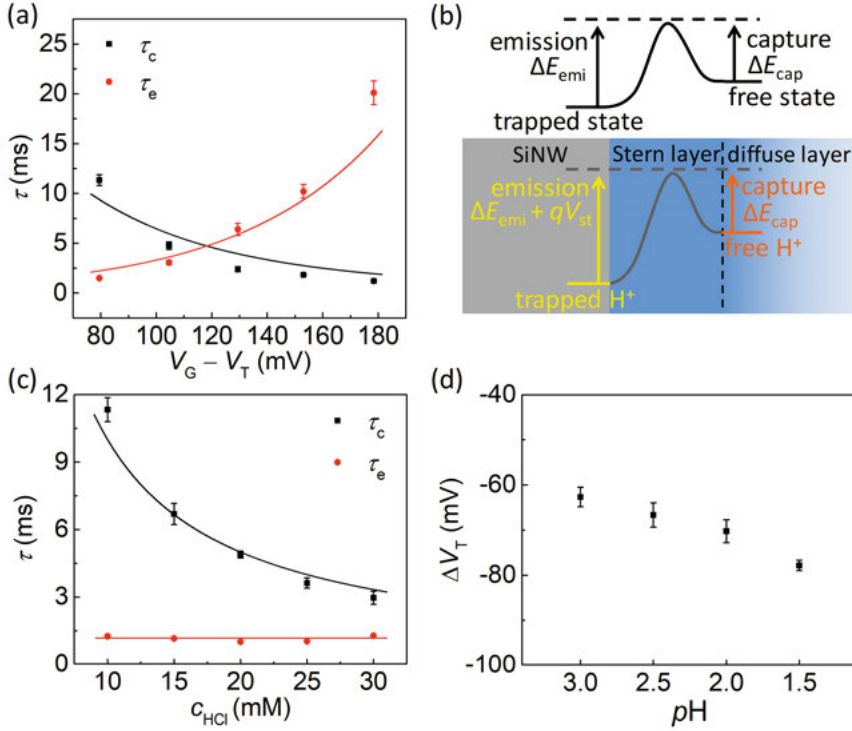


Figure 5.4. (a)  $\tau_c$  and  $\tau_e$  of Dev. A as a function of  $V_G - V_T$ . (b) Schematics of energy barriers of a general analyte-receptor reaction process (upper) and the  $\text{H}^+$ -DB interaction (lower). (c)  $\tau_c$  and  $\tau_e$  as a function of HCl concentration measured at  $I_{\text{DS}} = 40 \text{ nA}$ . (d) pH response of the SiNWFET measured in HCl solution. The solid curves in (a) and (c) are the fitting results.

According to the first-order Langmuir kinetics, considering an analyte-receptor reaction on a surface, the fraction of analyte bound receptor ( $\theta$ ) is determined by both capture and emission processes through [90]

$$\frac{d\theta}{dt} = k_{\text{on}} c_{\text{Hs}} (1 - \theta) - k_{\text{off}} \theta, \quad (5.1)$$

where  $k_{\text{on}}$  and  $k_{\text{off}}$  are the association and dissociation constants of the analyte-receptor reaction, respectively.  $k_{\text{on}}$  and  $k_{\text{off}}$  are determined by the kinetic energy barriers of the capture ( $\Delta E_{\text{cap}}$ ) and emission ( $\Delta E_{\text{emi}}$ ) processes, respectively (see the schematic illustration in Figure 5.4(b) (upper)). For the  $\text{H}^+$ -DB interaction, the potential drop across the Stern layer  $V_{\text{st}}$  adds an additional barrier  $qV_{\text{st}}$  to the  $\text{H}^+$  emission process, as illustrated in Figure 5.4(b) (lower). Therefore Eq. (5.1) is written as

$$\frac{d\theta}{dt} = k_{\text{on}} c_{\text{Hs}} (1 - \theta) - k_{\text{off}} e^{-\frac{qV_{\text{st}}}{kT}} \theta. \quad (5.2)$$

In the case of a single DB,  $\theta$  changes from 0 to 1 when a  $\text{H}^+$  ion is captured, and from 1 to 0 when the  $\text{H}^+$  ion is emitted.  $\tau_c$  and  $\tau_e$  of the single  $\text{H}^+$ -DB interaction can therefore be expressed as

$$\frac{1}{\tau_c} = k_{\text{on}} c_{\text{Hs}} \quad \text{and} \quad \frac{1}{\tau_e} = k_{\text{off}} e^{-\frac{qV_{\text{st}}}{kT}}. \quad (5.3)$$

The potential and charge distribution at SiNW/HCl interface (including  $c_{\text{Hs}}$  and  $V_{\text{st}}$ ) can be calculated numerically using the site-binding and Gouy-Chapman-Stern (GCS) models [57]. Detailed calculation method is available in **Paper III**. With the inputs of  $c_{\text{Hs}}$  and  $V_{\text{st}}$ , the measured time constants at different  $V_G$  can be fitted by Eq. (5.3), which is shown by the solid curves in Figure 5.4(a). Parameters  $C_{\text{st}}$ ,  $k_{\text{on}}$ , and  $k_{\text{off}}$  of Dev. A extracted from the fitting are listed in Table 5.1.

$\tau_c$  and  $\tau_e$  were also measured at different bulk HCl concentrations ( $c_{\text{HCl}}$ ) ranging from 10 to 30 mM at a fixed  $I_{\text{DS}} = 40$  nA, as shown in Figure 5.4(c). Here  $\tau_c$  becomes lower with increasing  $c_{\text{HCl}}$  while  $\tau_e$  is independent of  $c_{\text{HCl}}$ . Such dependence can be explained by the negligible pH sensitivity in the  $c_{\text{HCl}}$  range between 10 and 30 mM (pH 2–1.5 in Figure 5.4(d)), which indicates that the electrical potential across the EDL almost does not change in this pH range.  $c_{\text{Hs}}$  follows the increase of  $c_{\text{HCl}}$  to maintain a constant potential drop across the diffuse layer. Higher  $c_{\text{Hs}}$  will lead to a reduced  $\tau_c$  as analytically expressed in Eq. (5.3). On the other hand, since  $V_{\text{st}}$  does not change in this pH range either,  $\tau_e$  stays constant.

The relative amplitude ( $\Delta I_{\text{DS}}/I_{\text{DS}}$ ) at different  $V_G - V_T$  are plotted in Figure 5.5(a), where  $\Delta I_{\text{DS}}$  is the difference between the two peaks in  $I_{\text{DS}}$  histograms. As discussed in Chapter 2.1, both number ( $\Delta N/N$ ) and mobility ( $\Delta\mu/\mu$ ) fluctuations can contribute to  $\Delta I_{\text{DS}}/I_{\text{DS}}$ . The calculated contribution from  $\Delta N/N$  is shown in Figure 5.5(b), which is negligible comparing to the measured  $\Delta I_{\text{DS}}/I_{\text{DS}}$ . Details of the calculation are presented in **Paper III**. As a result,  $\Delta I_{\text{DS}}/I_{\text{DS}}$  is mainly ascribed to  $\Delta\mu/\mu$  due to the change of local Coulomb scattering strength induced by a single charge [62]:

$$\frac{\Delta I_{\text{DS}}}{I_{\text{DS}}} = \frac{\Delta\mu}{\mu} = \frac{\alpha_{\text{sc}} \mu}{A}. \quad (5.4)$$

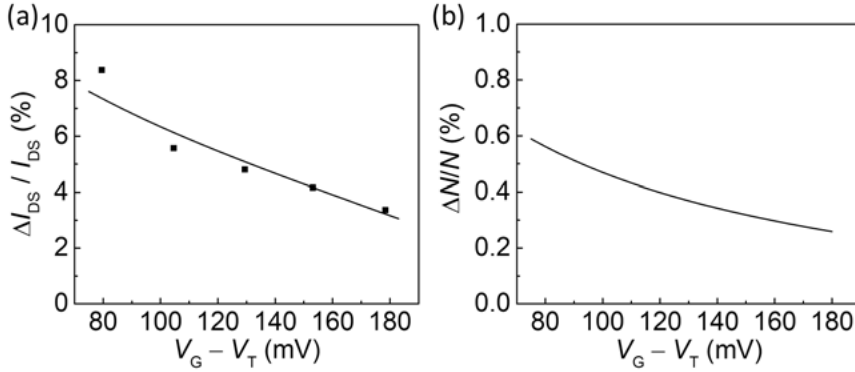


Figure 5.5. (a) Relative signal amplitude as a function of  $V_G - V_T$ . The solid curve is the fitting results. (b) Calculated contribution from number fluctuation.

$\Delta I_{DS}/I_{DS}$  decreases at higher  $V_G$ , which can be explained by the reduced mobility and scattering coefficient [91].  $\Delta I_{DS}/I_{DS}$  of Dev. A measured at different  $V_G$  can be well fitted with the mobility fluctuation, shown as the solid curve in Figure 5.5(a) (see **Paper III** for more details). The extracted scattering coefficient falls into the range of  $5.4\text{--}8.4 \times 10^{-15} \text{ V}\cdot\text{s}$ , which is in good agreement with the reported value [91].

Table 5.1. Parameters extracted from the fitting of time constants and signal amplitudes of Dev. A and B.

Parameters	Dev. A	Dev. B (DB 1)	Dev. B (DB 2)
$C_{st}$ ( $\text{F}\cdot\text{cm}^{-2}$ )	$4 \times 10^{-5}$	$4 \times 10^{-5}$	$4 \times 10^{-5}$
$k_{on}$ ( $\text{M}^{-1}\cdot\text{ms}^{-1}$ )	0.1	0.05	0.1
$k_{off}$ ( $\text{ms}^{-1}$ )	0.2	1.4	0.15
$\alpha_{sc}$ ( $\text{V}\cdot\text{s}$ )	$5.4\text{--}8.4 \times 10^{-15}$	$2.7\text{--}2.8 \times 10^{-15}$	$5.8\text{--}8.5 \times 10^{-15}$

### 5.3 One-by-one activation of DBs

It has been reported that in a MOSFET multiple carrier traps with different energy levels can be activated one-by-one through  $V_G$  modulation [92]. Similar one-by-one activation of DBs as  $H^+$  receptors on the SiNW, is also observed on our SiNWFET. Figure 5.6(a) and (b) present the  $I_{DS}$  traces and three representative histograms measured on a different SiNWFET (Dev. B), respectively. The traces can be separated in two groups depending on  $V_G$ . The first DB (DB 1) is activated at  $V_G - V_T = -12.6$  mV, where the DB empty state is dominating. With the increase of  $V_G$ , the occupation probability for DB 1 increases gradually. DB 1 is mostly filled with a  $H^+$  ion at  $V_G - V_T = 47.3$  mV. As  $V_G$  further increases, the second DB (DB 2) starts to interact with  $H^+$  at  $V_G - V_T = 82.3$  mV, and DB 2 shows a similar behavior with DB 1. For a clearer illustration, the occupation probability of the two DBs in the one-by-one activation process is plotted in Figure 5.6(c).

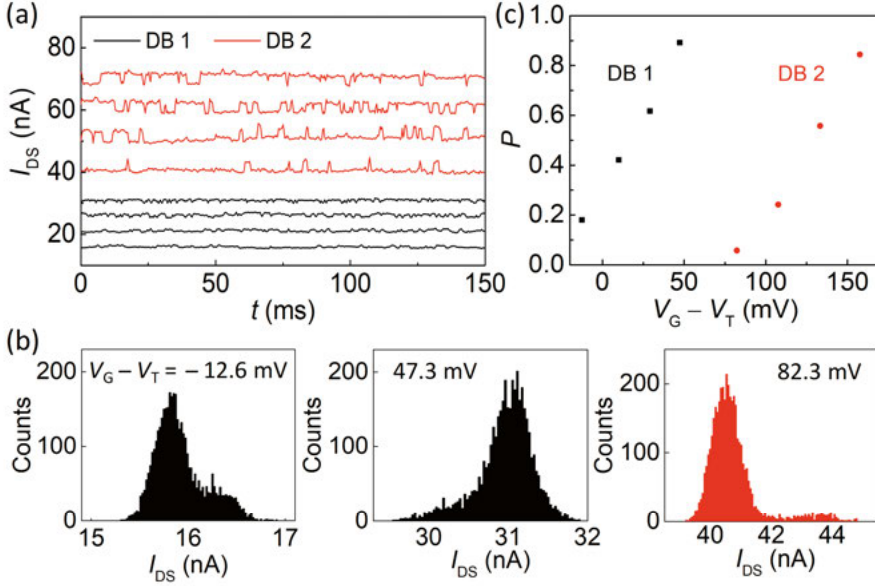


Figure 5.6. (a)  $I_{DS}$  sampling results at varied  $V_G - V_T$  in 10 mM HCl with a 3 kHz sampling frequency. (b) Three representative histograms of  $I_{DS}$ . (c) Occupation probability of the two DBs as a function of  $V_G - V_T$ .

$\tau_c$  and  $\tau_e$  of the two DBs of Dev. B at different  $V_G$  are plotted in Figure 5.7(a). The time constants can also be well fitted by Eq. (5.3) using the same  $C_{st}$  value as Dev. A, which verifies the validness of our explanation on the time constants of single  $H^+$ -DB interaction. The extracted fitting parameters are also listed in Table 5.1. The equilibrium constant  $K = k_{on}/k_{off}$  of the two DBs differs by  $\sim 20$  times, which corresponds to  $\sim 78$  mV difference in the

energy level between DB 1 and DB 2 in energy band gap. This energy difference is consistent with the difference of  $V_G$  to activate DB 1 and DB 2. As shown in Figure 5.7(b),  $\Delta I_{DS}/I_{DS}$  of both DBs can be well fitted with mobility fluctuation and the extracted scattering coefficient  $\alpha_{sc}$  are listed in Table 5.1.  $\Delta I_{DS}/I_{DS}$  differs largely of the two DBs, which further supports that they are distinct DBs. Although more than one DB might exist on the SiNW surface, they could be activated individually by  $V_G$  for single charge detection.

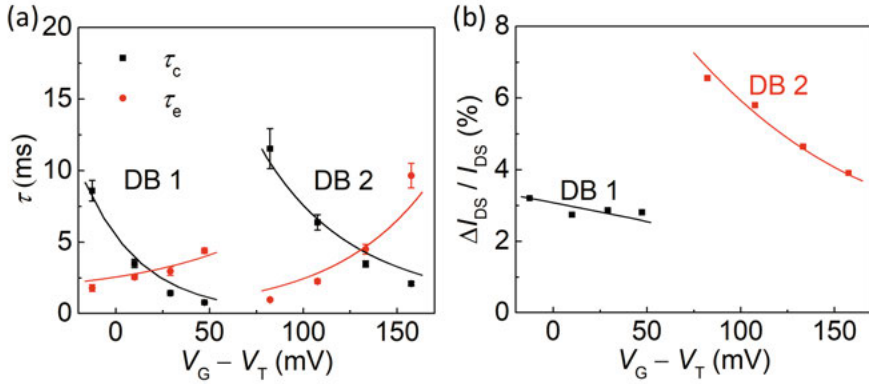


Figure 5.7. (a) Time constants and (b) relative signal amplitudes of the two DBs as a function of  $V_G - V_T$ . The solid curves are the fitting results.



## 6. SiNW Resonator for Quantum Sensing

The sensitive detection of ions using SiNWFETs has been discussed in Chapter 4 and 5. In this chapter, a doubly clamped SiNW based nanoelectromechanical resonator will be studied to investigate its applications for quantum sensing at low temperature.

The SiNW resonator exhibits a high resonant frequency  $f_0 = 3$  GHz at the temperature of 20 mK, resulting in a calculated thermal phonon occupancy  $n_{\text{ph}}$  much below the quantum limit ( $n_{\text{ph}} \ll 1$ ). A quality factor  $Q \sim 1000$  is extracted, which suggests a good isolation between the mechanical vibration and its thermal environment ( $f_0 Q \gg kT/h$ ). A low effective mass  $m_{\text{eff}}$  of the tiny SiNW leads to a large zero-point motion  $x_{\text{zp}} \sim 0.2$  pm. Both  $f_0$  and  $x_{\text{zp}}$  reach the best level among the state-of-the-art doubly clamped NW resonators using Si-containing materials. The SiNW resonator can also act as a single-hole transistor (SHT), which is confirmed by the observed Coulomb diamond transportation features. The single-hole tunneling behaviors are strongly correlated to the mechanical vibration, which enables the fully electrical readout of the mechanical signal. The dominating signal transduction mechanism is ascribed to the piezoresistive effect. Moreover, an apparent effective piezoresistive gauge factor of the device ( $g \sim 6000$ ) is among the largest reported gauge factors of Si.

### 6.1 3 GHz SiNW resonator

As shown in Figure 6.1, a SiNW with 17 nm in width, 27 nm in thickness, and 200 nm in length is suspended, with a suspension height of 30 nm to the underneath substrate. The SiNW consists of 100-nm-long lightly  $p$ -type region at the center and 50-nm-long heavily  $p$ -type regions at both ends. The lightly  $p$ -type region of the SiNW is gated by a 140-nm-wide side gate with a 55 nm gap. The conductance of the SiNW channel can be modulated by a DC voltage applied on the side gate  $V_G$ . The electrical and mechanical properties

of the device are characterized in a dilution refrigerator with a base temperature of 20 mK and chamber pressure of  $10^{-7}$  Torr.

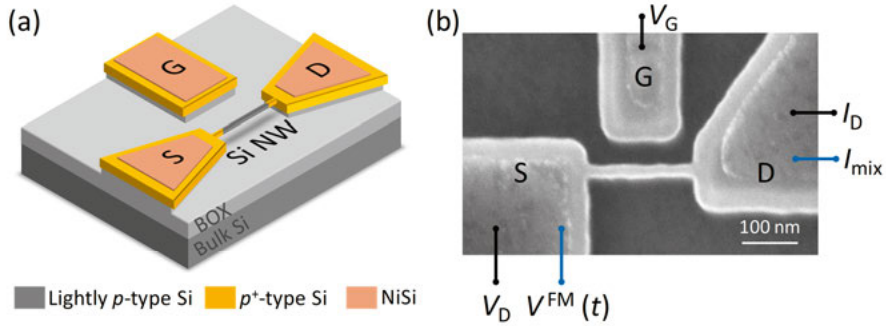


Figure 6.1. (a) Schematic and (b) SEM image and schematic measurement arrangement of the SiNW resonator.

The vibration measurement arrangement is illustrated in Figure 6.1(b). Mechanical vibration of the SiNW is actuated and detected by using a one-source frequency-modulation (FM) technique [93]. The S terminal is biased by a DC voltage  $V_D$  superimposed by an AC FM signal  $V^{FM}(t)$  with a driven frequency  $f_d$ . The side gate terminal is biased by  $V_G$ . Mixing current ( $I_{mix}$ ) is detected with a lock-in amplifier at the D terminal. Details of the vibration measurement arrangement are available in **Paper IV**.

Figure 6.2(a) shows the measured  $I_{mix}$  as a function of  $f_d$  at side gate voltage  $V_G = -25$  V with a driving power  $P_d = -41$  dBm. A resonant frequency  $f_0 = 2.9997$  GHz and a quality factor  $Q = 1249$  are extracted from the  $I_{mix}$  curve with data fitting. Figure 6.2(b) plots the resonance peaks of  $I_{mix}$  at  $V_G = -25$  V with a series of  $P_d$  from  $-31$  to  $-19$  dBm. It is clearly indicated that a higher  $P_d$  not only broadens the resonance peak but also lowers the resonant frequency. Such nonlinearity is commonly observed in nanoscale mechanical resonators [93], [94]. The higher driving power, which induces a larger vibration amplitude, will modify both the stiffness of the SiNW and the energy dissipation of the resonator.

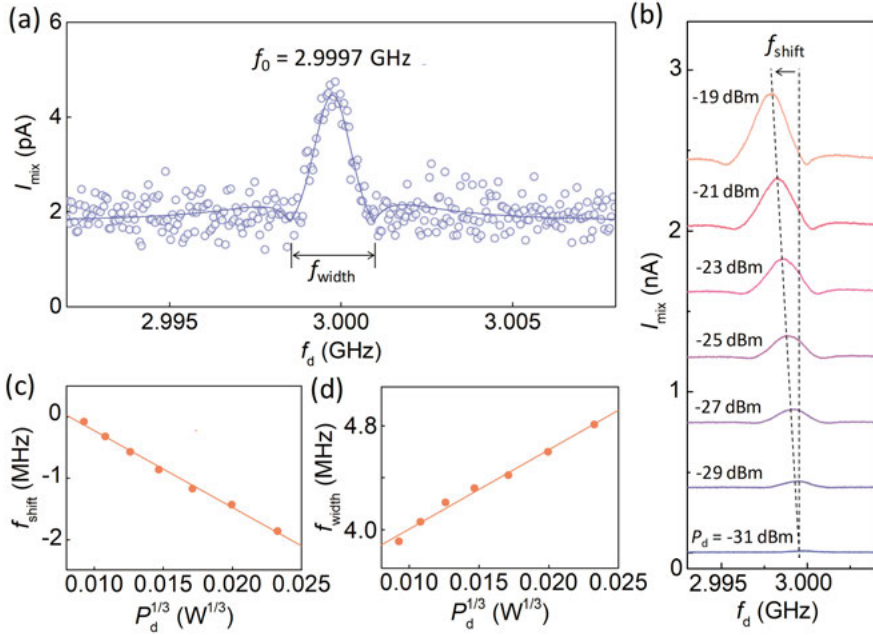


Figure 6.2. (a)  $I_{\text{mix}}$  as a function of driving frequency at  $V_G = -25$  V and  $P_d = -41$  dBm. (b)  $I_{\text{mix}}$  as a function of driving frequency with different  $P_d$  at  $V_G = -25$  V. Each data set is offset by 0.4 nA for clarity. Extracted (c) shift and (d) width of the resonance peaks as a function of cube root of  $P_d$ .

To further analyze the nonlinearity, shift ( $f_{\text{shift}}$ ) and width ( $f_{\text{width}}$ ) of the resonance peaks in Figure 6.2(b) are plotted versus  $P_d^{1/3}$  (see Figure 6.2(c) and (d), respectively). The linear fitting results show that both  $f_{\text{shift}}$  and  $f_{\text{width}}$  are proportional to  $P_d^{1/3}$ , which indicates that the nonlinear terms are dominated by a Duffing term ( $\alpha x^3$ , where  $x$  is the displacement of the resonator) and a van der Pol nonlinearity ( $\eta x^2 dx/dt$ ) [94].

## 6.2 Single-hole transistor behavior

Our device also acts as a single-hole transistor, in which the hole tunnels through the channel one by one due to Coulomb repulsion [95]. The SHT behavior is demonstrated by the profile in Figure 6.3(a) at  $V_D = 1$  mV, which shows a typical characteristic of Coulomb oscillations. As shown in Figure 6.3(b) (left), the measured  $I_{\text{DS}}$  at different  $V_D$  and  $V_G$  exhibits a typical quantum-dot-like Coulomb diamond feature. Electrochemical potential of the quantum dot ( $\mu_{\text{QD}}$ ) is quantized to a series of discrete energy levels separated by charging energy. Illustrations in Figure 6.3(b) (right) present different configurations of  $\mu_{\text{QD}}$  and Fermi levels of source ( $\mu_S$ ) and drain ( $\mu_D$ ) terminals. When  $\mu_{\text{QD}}$  lies in the bias window between  $\mu_S$  and  $\mu_D$ , a hole can

tunnel through the quantum dot, thus a current can be detected between source and drain. However, when  $\mu_{\text{QD}}$  is out of the window between  $\mu_{\text{S}}$  and  $\mu_{\text{D}}$ , no current can flow through the quantum dot. Since the relative position of  $\mu_{\text{QD}}$  to the window between  $\mu_{\text{S}}$  and  $\mu_{\text{D}}$  is determined by both  $V_{\text{G}}$  and  $V_{\text{D}}$ ,  $I_{\text{DS}}$  oscillates with the varying  $V_{\text{G}}$  at a fixed  $V_{\text{D}}$ .

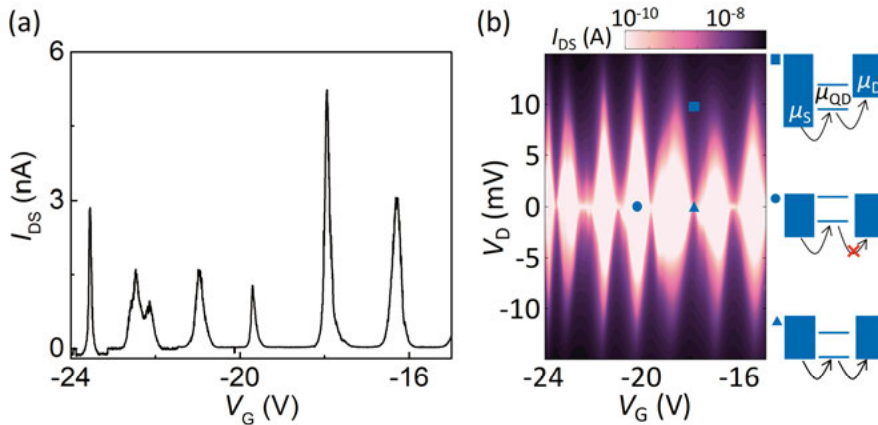


Figure 6.3. (a)  $I_{\text{DS}}$  as a function of  $V_{\text{G}}$  at  $V_{\text{D}} = 1 \text{ mV}$ . (b)  $I_{\text{DS}}$  as a function of  $V_{\text{G}}$  and  $V_{\text{D}}$ . Illustrations in the right column show the relative electrochemical potentials between S/D and quantum dot.

### 6.3 Transduction mechanism analysis

The DC voltage on the side gate  $V_{\text{G}}$  applies an electrostatic force to the SiNW, which can modulate the strain and the resonant frequency of the SiNW. As shown in Figure 6.4(a), to investigate the  $V_{\text{G}}$  modulation effect, the mixing current  $I_{\text{mix}}$  is monitored when  $V_{\text{G}}$  is varied from  $-25$  to  $-15 \text{ V}$  and  $P_{\text{d}}$  is fixed at  $-33 \text{ dBm}$ . The resonant frequency can be tuned by  $5 \text{ MHz}$  when  $V_{\text{G}}$  is changed from  $-25$  to  $-15 \text{ V}$ .

The mechanical vibration can be transduced to the electrical signal through piezoresistive effect [93] and/or field-effect [96]. It has been shown that  $I_{\text{mix}}$  should be proportional to conductance if the transduction mechanism is based on piezoresistive effect, i.e.,  $I_{\text{mix}}^{\text{PZT}} \propto G$ , while it be proportional to transconductance if the transduction mechanism is due to field-effect, i.e.,  $I_{\text{mix}}^{\text{FET}} \propto dG/dV_{\text{G}}$ . To understand transduction mechanism of our SiNW resonator, both  $I_{\text{DS}}$  and  $I_{\text{mix}}$  at resonance, i.e.,  $I_{\text{mix}}^{\text{res}}$ , are measured simultaneously with changing  $V_{\text{G}}$ , as shown in Figure 6.4(b) and (c).  $I_{\text{mix}}^{\text{res}}$  and  $I_{\text{DS}}$  show similar oscillation behaviors with varying  $V_{\text{G}}$ , and reach their peak values at the same  $V_{\text{G}}$ . Therefore, we attribute the dominating signal transduction mechanism in the SiNW resonator to the piezoresistive effect.

This behavior is in sharp contrast to field-effect transduction mechanism reported in carbon nanotube resonators, where  $I_{\text{mix}}^{\text{res}}$  peaks appear where  $dI_{\text{DS}}/dV_G$  reaches its peaks [97].

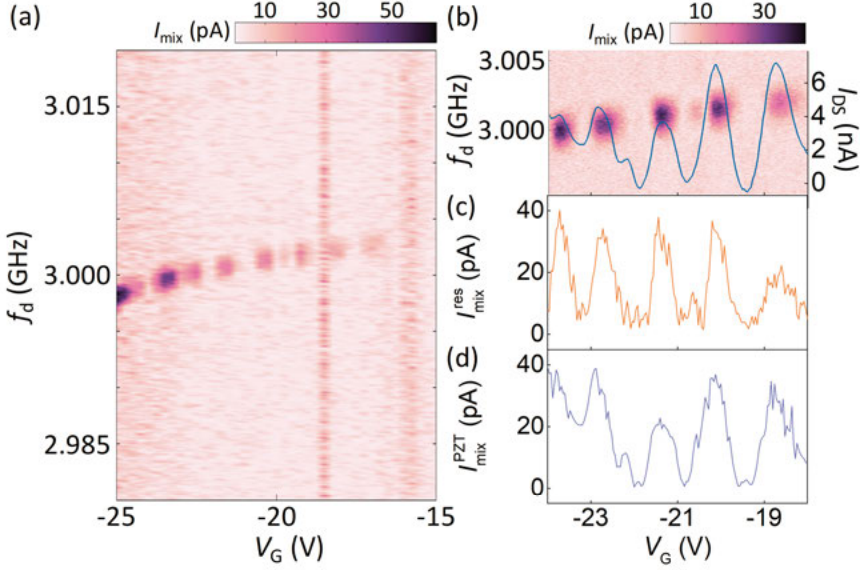


Figure 6.4. (a)  $I_{\text{mix}}$  as a function of gate voltage and driving frequency at  $P_d = -33$  dBm. (b) Zoom-in figure of (a), where the blue curve is  $I_{\text{DS}}$  simultaneously measured with  $I_{\text{mix}}$ . (c) Mixing current at resonance as a function of  $V_G$ . (d) Calculated mixing current at resonance based on piezoresistive effect as a function of  $V_G$ , with an estimated effective gauge factor  $g = 6000$ .

$I_{\text{mix}}$  transduced from piezoresistive effect is proportional to the piezoresistive gauge factor ( $g$ ). However,  $g$  of Si shows a strong dependence on many parameters, such as crystallographic orientation, device dimensions, carrier density, and temperature [98]-[100]. To estimate the effective  $g$  of our device, the mixing currents at resonance are calculated with different  $g$  values and compared with the measured  $I_{\text{mix}}^{\text{res}}$ . As shown in Figure 6.4(d), a giant effective  $g$  value about 6000 is needed to reach the measured  $I_{\text{mix}}^{\text{res}}$  at  $P_d = -33$  dBm with the appearance of Coulomb oscillations. This giant effective  $g$  is among the largest reported gauge factors of Si [98], [99], [101]. One possible reason could be that the SiNW resistance is dominated by the tunneling barriers at  $P_d = -33$  dBm and the tunneling resistance might be more sensitive to the mechanical strain. In addition, the effective  $g$  has a strong dependence on carrier density at nanoscale. The effective carrier density in our device is lower when the transport behavior is dominated by single-hole tunneling (the appearance of Coulomb oscillations) at  $P_d = -33$  dBm. It is worth noting that although the dominating signal transduction

mechanism is the piezoresistive effect, a more complicated mechanism cooperated by both piezoresistive and field effects, especially in the single-hole tunneling regime, might be behind the real signal transduction and is to be further investigated.

## 7. Lateral BJTs as Local Signal Amplifiers

As discussed in Chapter 2.3, to suppress external interference, a bipolar junction transistor (BJT) can be used as a local current amplifier of SiNW electronic sensor. However, the conventional vertical BJT, which requires micrometer-thick Si, is not technologically compatible with the SiNW devices fabricated on SOI substrate.

In Chapter 7, lateral version of BJTs (LBJTs) are designed and fabricated on SOI substrate to study their potential application as local signal amplifiers for SiNW electronic sensors. Chapter 7.1 presents a CMOS-compatible fabrication process of the LBJT and the current gain ( $\beta$ ). Chapter 7.2 exhibits a systematic study of the substrate voltage ( $V_{\text{sub}}$ ) modulation effect of the current-voltage ( $I$ - $V$ ) characteristics and current noise of the LBJT.

### 7.1 Device fabrication and characterization

A cross-sectional schematic of an LBJT on SOI substrate is shown in Figure 7.1(a). The LBJT is of  $n^+$ - $p$ - $n^+$  type with a poly-Si contact on top of the base (B). The emitter (E) and collector (C) are symmetric in terms of doping level and geometry. An effective E/C doping level  $N_D = 1.5 \times 10^{20} \text{ cm}^{-3}$  and B doping level  $N_A = 8 \times 10^{17} \text{ cm}^{-3}$  are estimated by sheet resistance measurements. A 20-nm-thick thermal oxide layer (barrier oxide) acts as the etching stop layer for poly-Si and the electrical isolation layer between poly-Si and E/C. A series of base width ( $W_B$ ) are designed to study its influence on  $\beta$ . A cross-sectional TEM image of the LBJT is presented in Figure 7.1(b). Before any electrical measurement, the LBJT was annealed in forming gas to remove charged traps near Si/oxide interfaces.

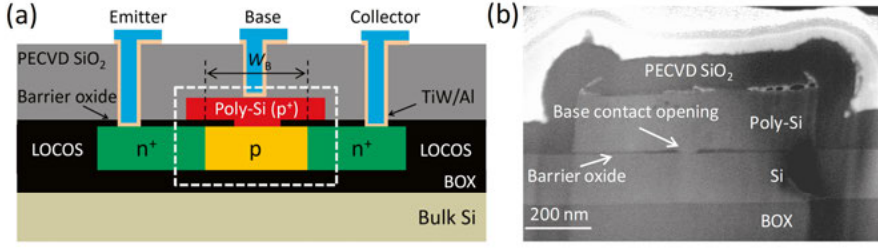


Figure 7.1. Cross-sectional (a) schematic and (b) TEM image of an LBJT on SOI substrate. The TEM image is referred to the region in the dashed rectangle in (a).

Figure 7.2(a) shows a typical Gummel characteristics and current gain of the LBJT with  $W_B = 50$  nm measured at collector voltage  $V_C = 1$  V. The collector ( $I_C$ ) and base ( $I_B$ ) currents are modulated by base voltage ( $V_B$ ) with slopes of 61.2 and 74.8 mV/dec in  $V_B$  range from 0.4 to 0.9 V, respectively. The non-ideal slope of  $I_B$  could be ascribed to the presence of defects in the E-B space charge region (SCR) and near the Si/oxide interfaces, which are not completely removed by FGA [102]. This leads to a non-flat  $\beta$  which strongly depends on  $V_B$  with a maximum value of  $\beta_{\max} = 70$  at  $V_B = 0.85$  V.  $\beta_{\max}$  of the LBJTs with different base width is summarized in Figure 7.2(b). Clearly, a higher  $\beta_{\max}$  can be achieved on the LBJT with a narrower base.

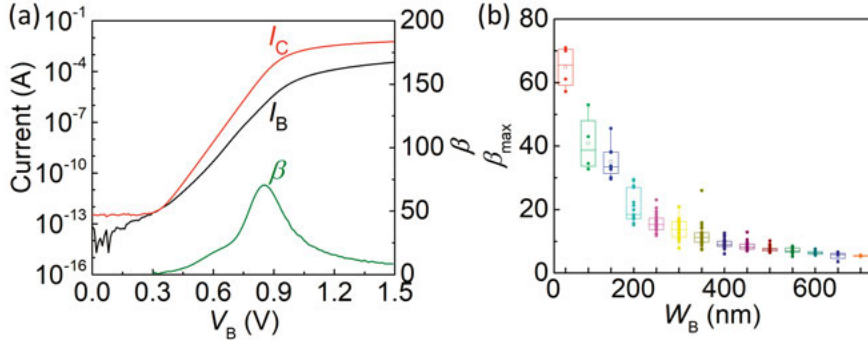


Figure 7.2. (a) Gummel characteristics and  $\beta$  of the LBJT with  $W_B = 50$  nm.  $V_C = 1$  V. (b)  $\beta_{\max}$  of the LBJTs with different  $W_B$ .

## 7.2 Substrate voltage modulation

As illustrated in Figure 7.3(a) and (b), a positive  $V_{\text{sub}}$  applied on bulk Si can induce a depletion layer and bend the Si energy diagram downwards by  $q\psi_s$  in the base region near the Si/BOX interface. A positive  $V_B$  lowers the E-B injection barrier and thus increases electron injection current into the base bulk



(annotated by  $I_{C-B}$  in Figure 7.3(a)). Similarly, the E-B injection barrier can also be lowered by a positive  $V_{\text{sub}}$  (indicated in Figure 7.3(c)), which leads to an increase of electron injection current into the base near the Si/BOX interface as annotated by  $I_{C-I}$  in Figure 7.3(a).

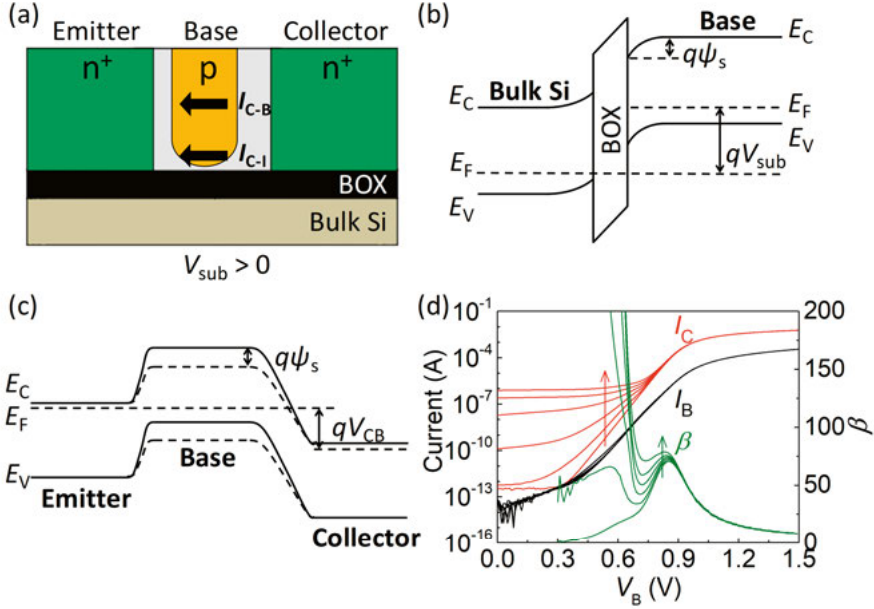


Figure 7.3. (a) Cross-sectional schematic of depletion region in the base (grey area) and different  $I_C$  components. (b) and (c) Band diagrams with  $V_{\text{sub}} > 0$ .  $\psi_s$  in (c) is the surface potential at the Si/BOX interface as shown in (b). (d) Gummel characteristics and  $\beta$  measured at different  $V_{\text{sub}}$  at  $V_C = 1$  V. The arrows indicate  $V_{\text{sub}}$  increase from 0 V to 10 V with a fixed step of 2 V.

Modulation effect of the positive  $V_{\text{sub}}$  is exhibited in Figure 7.3(d).  $I_C$  and  $\beta$  increase considerably with  $V_{\text{sub}}$  especially when  $V_B$  is lower than 0.8 V. Such increase can be ascribed to the  $V_{\text{sub}}$ -enhanced E-B current injection near the Si/BOX interface. On the other hand,  $I_B$  is insensitive to  $V_{\text{sub}}$ , suggesting that the recombination current generated near the Si/BOX interface does not contribute significantly to  $I_B$ . Taking  $V_{\text{sub}} = 4$  V as an example, the  $I_C$  curve can be divided into three regions depending on  $V_B$ . When  $V_B < 0.3$  V,  $I_C$  is dominated by  $I_{C-I}$ , which shows a weak dependence of  $V_B$ . Evidently, the LBJT should not be operated in such bias range for effective signal amplification. As  $V_B$  increases,  $I_{C-B}$  increases exponentially and its contribution to  $I_C$  rises. An improved  $V_B$  control of  $I_C$  is observed in the  $V_B$  range from 0.3 to 0.8 V. This range is beneficial for current signal amplification. For  $V_B > 0.8$  V,  $I_C$  is dominated by  $I_{C-B}$  and thus is under a negligible modulation by  $V_{\text{sub}}$ . Clearly, the  $V_B$  range advantageous for signal

amplification is curbed with the increased  $V_{\text{sub}}$ . More discussion of  $V_{\text{sub}}$  modulation effect of  $I_C$  can be found in **Paper VI**.

The  $V_{\text{sub}}$  modulation of  $I_C$  and  $I_B$  noise,  $S_{IC}$  and  $S_{IB}$ , was also characterized.  $S_{IC}$  at 10 Hz measured at different  $V_{\text{sub}}$  is shown in Figure 7.4(a). In the low  $I_C$  range,  $I_C$  is dominated by  $I_{C-I}$  near the Si/BOX interface. The random carrier trapping and detrapping processes to the traps near the Si/BOX interface will generate extra noise to  $S_{IC}$ . The noise of  $I_{C-I}$  is indicated by the grey dashed line, measured at  $V_B = 0$  V ( $I_C = I_{C-I}$ ). As  $I_C$  increases, it eventually becomes dominated by  $I_{C-B}$  and thus  $S_{IC}$  falls in the black dashed line measured at  $V_{\text{sub}} = 0$  V.

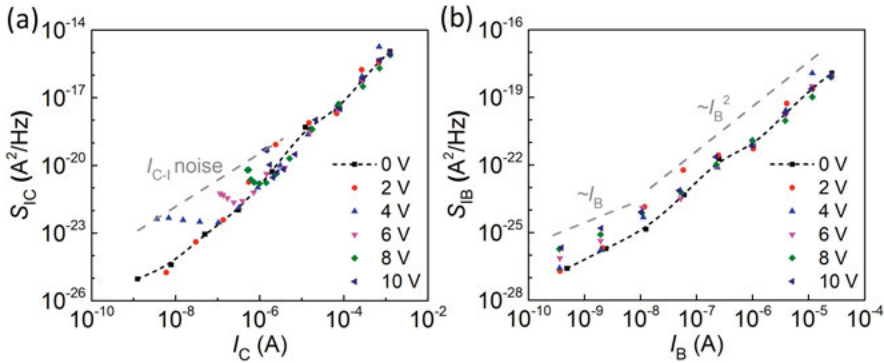


Figure 7.4. (a)  $S_{IC}$  at 10 Hz as a function of  $I_C$  measured at different  $V_{\text{sub}}$ .  $I_{C-I}$  noise indicates  $S_{IC}$  measured at  $V_B = 0$  V. (b)  $S_{IB}$  at 10 Hz as a function of  $I_B$  measured at different  $V_{\text{sub}}$ .

Figure 7.4(b) plots  $S_{IB}$  at 10 Hz as a function of  $I_B$  measured at different  $V_{\text{sub}}$ . At  $V_{\text{sub}} = 0$  V,  $S_{IB}$  shows an  $I_B^2$  dependence in a wide  $I_B$  range over 4 orders of magnitudes [103]. Such dependence could be ascribed to local fluctuations of electrical field associated with charging and discharging of the bulk defects in the E-B space charge region, which modulates the current flowing across the space charge region [104]. At  $V_{\text{sub}} > 0$  V,  $S_{IB}$  deviates from the  $I_B^2$  dependence and tends to be proportional to  $I_B$  in the range of  $I_B < 10^{-7}$  A. Referring to the Gummel plots in Figure 7.3(d) again,  $I_C$  is dominated by  $I_{C-I}$  under such bias conditions and therefore the main noise source is the random carrier trapping and detrapping processes near the Si/BOX interface [105], [106]. Our results reveal a transition process of noise source in the LBJT when the dominant  $I_C$  contribution is shifted from the base bulk to the Si/BOX interface.

Although  $V_{\text{sub}}$  can significantly improve  $\beta$  at low  $V_B$ , it tends to induce extra noise near the Si/BOX interface. This extra noise is reflected in  $S_{IB}$  at  $I_B < 10^{-7}$  A. To apply the LBJT as a local signal amplifier for the SiNW electronic sensor, it is essential that the input-referred noise, *i.e.*,  $S_{IB}$ , of the LBJT is significantly lower than that of the SiNW sensor. Consequently,

setting an appropriate  $V_{\text{sub}}$  at a given input current ( $I_{\text{B}}$ ) is important in order to ensure an optimal overall SNR.

## 8. Conclusions and Future Perspectives

The purpose of this thesis is to explore the SiNW electronic devices, *i.e.*, SiNWFETs and SiNW resonators, for different sensing applications. To pursue this goal, a CMOS-compatible fabrication process is optimized to downscale the SiNW dimensions to  $\sim 10$  nm. Meanwhile, the intrinsic noise of such downscaled device is suppressed, which is essential for achieving a high SNR. Afterwards, different sensing applications of our SiNW electronic devices are studied and summarized as follow:

1. Multiplexed detection of molecular and elemental ions is demonstrated using a SiNWFET array. The SiNWFET array is separately functionalized with the MMMs as the sensing layers of the target ions, *i.e.*,  $\text{MB}^+$  and  $\text{Na}^+$ . Using the same type of sensing layers for both targets greatly simplifies the integration process. Both  $\text{MB}^+$ - and  $\text{Na}^+$ -sensors show near-Nernstian responses in wide target concentration ranges. The  $\text{MB}^+$ -sensor further shows an excellent selectivity against common interfering ions in liquid samples, *e.g.*,  $\text{H}^+$ ,  $\text{Na}^+$ , and  $\text{K}^+$ . However, the  $\text{Na}^+$ -sensor is more susceptible to the presence of  $\text{MB}^+$  due to the hydrophobic interaction between  $\text{MB}^+$  and PVC matrix of the  $\text{Na}^+$ -MMM. Such interaction generates a large interference to  $\text{Na}^+$  sensing once the concentration of  $\text{MB}^+$  exceeds a threshold value. Based on the observed cross-interference of the two target ions, multiplexed detection of  $\text{MB}^+$  and  $\text{Na}^+$  is demonstrated in a single sample solution, in which the concentration of  $\text{MB}^+$  is controlled below the threshold.

2. PEG is doped into the MMM to improve its selectivity and expand the multiplexed detection range. In order to address the hydrophobic interaction between  $\text{MB}^+$  and PVC matrix, the hydrophilic PEG is selected as the additive into the MMM to suppress its hydrophobicity. It is verified that PEG doping can reduce the MMM's affinity to hydrophobic  $\text{MB}^+$ , leading to a much reduced interference from the hydrophobic interaction to the  $\text{Na}^+$ -MMM. Such effects are evidenced by the significantly improved selectivity coefficients of the PEG-doped  $\text{Na}^+$ -MMMs against  $\text{MB}^+$ . The improved selectivity of the  $\text{Na}^+$ -sensor expands the dynamic range of the multiplexed detection by one order of magnitude.

3. Direct detection of a single  $\text{H}^+$  is achieved using gate oxide free sub-10 nm SiNWFETs. The SiNWFETs are fabricated using an optimized CMOS-compatible process. A  $\text{H}_2$  annealing process is explored to smooth the SiNW surface to reduce the surface defect density and the intrinsic device noise. Si DBs on the SiNW surface act as  $\text{H}^+$  receptors. The majority of DBs are

passivated by buffered HF with covalent H-terminations, leaving a single activated DB on the tiny SiNW surface for single  $H^+$  detection. The single  $H^+$ -DB interaction generates  $I_{DS}$  switching signals by modulating the local Coulomb scattering strength. Based on the detected signals, kinetics of the single  $H^+$ -DB interaction and its correlation to the energy barriers at the SiNW/electrolyte interface are systematically investigated. This work demonstrates the unprecedented ability of our SiNWFET to investigate the physics of solid/liquid interface at single charge level.

4. A suspended 3 GHz SiNW nanoelectromechanical resonator is developed aiming for electrical detection of potential quantized mechanical vibration at low temperature. The doubly clamped SiNW resonator is fabricated on SOI substrate. Such SiNW resonator achieves a resonant frequency of 3 GHz, reaching the best level among the state-of-the-art SiNW resonators. A single-hole tunneling behavior is also observed in the resonator, which shows a strong correlation with the resonance signal. The dominating transduction mechanism is attributed to the piezoresistive effect. A giant effective  $g \sim 6000$  with a strong correlation to the single-hole tunneling is estimated from our measurements. This hybrid device is promising to investigate macroscopic quantum behaviors of vibration phonon mode.

5. Symmetric LBJTs are fabricated on SOI wafer as local current amplifiers for the SiNW electronic sensors. With the base width of 50 nm, a current gain of 70 is achieved with good reliability. For an  $n^+-p-n^+$  type LBJT, an improvement of  $\beta$  is observed by applying a positive  $V_{sub}$ , which can enhance the E-B current injection near the Si/BOX interface. However, carrier random trapping and detrapping processes in the vicinity of the Si/BOX interface would increase the LBJT device noise when the interface current contribution to  $I_C$  is significant. Applying an appropriate  $V_{sub}$  can both improve  $\beta$  and achieve an optimal overall SNR.

Based on the work in this thesis, basic knowledge and technique are accumulated about the CMOS-compatible fabrication and electrical characteristics of SiNW devices, ion-sensitive MMM, single charge analysis, high-frequency resonator, and amplification performance of LBJT. More efforts need be done to explore the sensing applications of SiNW electronic devices.

1. Microfluidics system should be integrated with the SiNWFET for real sensing applications. In this thesis, a polydimethylsiloxane (PDMS) container is used to hold the liquid sample for characterizing the sensing performance of the SiNWFET sensor. The microfluidics system will enable a more precise control of liquid sample delivery.

2. Surface functionalization method needs to be explored on the gate oxide free SiNW surface for single charge analysis of analytes other than  $H^+$ . The receptor of  $H^+$  in this thesis is the self-formed Si DB on the SiNW surface. To detect and analyze a single ion or molecule of other chemical and biological

species, one should explore the approach to functionalize the individual specific receptors on the SiNW surface.

3. More study needs to be conducted to investigate the transduction mechanism of the SiNW resonator. A more complicated mechanism, cooperated by both piezoresistive and field effects, might be hidden in the single-hole tunneling regime. Joint contributions from piezoresistive and field effects could provide rich physics of interaction between mechanical vibration and carrier transport. Furthermore, quantum-dot-based qubit can be defined in our system with a multiple-gate architecture, leading to a hybrid system consisting of solid-state qubits and high-frequency vibrational phonons. Such system could enable the investigation of many quantum effects, such as phonon number counting and coherent state transfer.

4. LBJs will be integrated with the SiNW sensors to suppress the environmental interference. In this thesis, the fabrication process of the LBJ is established and the characteristics of current gain and noise are studied. Integration of the LBJs and the SiNW sensors will be further explored on SOI substrates.

# Sammanfattning på Svenska

Kiselnanotråds (SiNW) baserade elektroniska enheter tillverkade med en kompletterande metall-oxid-halvledare (CMOS) kompatibel process har ett brett spektrum och lovande applikationer inom avkänningsområdet. Dessa SiNW-sensorer har hög känslighet, möjlighet till massproduktion till låga kostnader och hög integreringstäthet. I denna avhandling designar och tillverkar vi elektroniska SiNW-enheter genom den CMOS-kompatibla processen för kisel-på-isolatorskivor (SOI) och undersöker deras applikationer för jonavkänning och kvantavkänning.

För att uppnå detta mål optimerades den CMOS-kompatibla tillverkningsprocessen för att minska SiNW-dimensionerna till  $\sim 10$  nm. Under tiden tystades det inneboende bullret från en sådan minskad enhet, vilket är grundläggande för att uppnå en hög signal-till-brus förhållande (SNR). Därefter studerades olika avkänningsapplikationer för våra elektroniska SiNW-enheter, som kan sammanfattas enligt följande:

1. Multiplexerad detektion av molekylära och elementära joner demonstrerades på SiNWFET-system. SiNWFET tilldelades separat en funktion av blandat matrismembran (MMM) som avkänningsskikt för dummymål, *dvs.*  $\text{MB}^+$  och  $\text{Na}^+$ . Att använda samma typ av avkänningsskikt för båda målen förenklar integrationsprocessen avsevärt. Både  $\text{MB}^+$ - och  $\text{Na}^+$ -sensorer visar ett nästan Nernst-svar inom breda intervall av analytkoncentrationer.  $\text{MB}^+$ -sensorn visar vidare en utmärkt selektivitet mot vanliga störande joner i flytande prover,  $\text{H}^+$ ,  $\text{Na}^+$  och  $\text{K}^+$ . Emellertid är  $\text{Na}^+$ -sensorn mer mottaglig för närvaron av  $\text{MB}^+$  på grund av den hydrofoba interaktionen mellan  $\text{MB}^+$  och PVC-matrisen för MMM. En sådan interaktion genererar störningar för  $\text{Na}^+$ -avkänning när koncentrationen av  $\text{MB}^+$  överstiger tröskelvärdet. Baserat på den observerade korsinterferensen hos de två måljonerna demonstrerades multiplexerad detektion av  $\text{MB}^+$  och  $\text{Na}^+$  i en enda provlösning, där koncentrationen av  $\text{MB}^+$  kontrollerades under tröskelvärdet.

2. PEG dopades in i MMM för att förbättra dess selektivitet och utvidga det multiplexerade detekteringsområdet. För att ta itu med den hydrofoba interaktionen mellan  $\text{MB}^+$  och PVC-matrisen valdes den hydrofila PEG som tillsats i MMM för att undertrycka dess hydrofoba egenskaper. Det verifierades att PEG-dopning kunde minska MMM affinitet till hydrofob  $\text{MB}^+$ , vilket ledde till en mycket reducerad störning från de hydrofoba interaktionerna för den MMM-baserade  $\text{Na}^+$ -sensorn. Sådana effekter

bevisades av de signifikant förbättrade selektivitetskoefficienterna för  $\text{Na}^+$ -sensorerna mot  $\text{MB}^+$ . Den förbättrade selektiviteten hos  $\text{Na}^+$ -sensorn utvidgade det dynamiska området med en storleksordning vid multiplexerad detektion av  $\text{MB}^+$ - och  $\text{Na}^+$ -joner.

3. Direkt detektering av enstaka  $\text{H}^+$  uppnåddes på oxidfria SiNWFET-grindar under 10 nm. SiNWFET-enheterna tillverkades med en optimerad CMOS-kompatibel process. En  $\text{H}_2$ -glödningsprocess användes för att släta ut SiNW-ytan för att minimera densiteten av ytdefekter och enhetens inneboende ljud. Si-dinglande obligationer (DBs) på SiNW-ytan fungerar som  $\text{H}^+$ -receptorer. Majoriteten av DBs passiviserades genom BHF-etsning med kovalent H-terminering, vilket lämnade en enda aktiverad DB på den lilla SiNW-ytan för den enda  $\text{H}^+$ -detekteringen. Den enda  $\text{H}^+$ -DB-interaktionen genererade drain-source strömmen växlingssignaler genom att modulera den lokala Coulomb-spridningsstyrkan. Baserat på de detekterade signalerna genomfördes en systematisk undersökning av kinetiken för den enskilda  $\text{H}^+$ -DB-interaktionen och dess korrelation till energibarriärerna vid fast/elektrolyt-gränssnittet. Detta arbete visar en oöverträffad förmåga hos vårt SiNWFET att undersöka fysiken i gränssnittet mellan fast och flytande vid en enda laddningsnivå.

4. Upphängda 3 GHz SiNW nanoelektromekaniska resonator utvecklades med sikte på elektrisk detektering av potentiella kvantiserade mekaniska vibrationer vid låg temperatur. En dubbelklämd SiNW-resonator tillverkades på ett SOI-substrat. Denna SiNW-resonator uppnådde en resonansfrekvens på 3 GHz, vilket är den bästa nivån bland de senaste SiNW-resonatorerna. Ett enkelhåls-tunnelbeteende observerades också i resonatorn, vilket visade en stark korrelation med resonanssignalen. Den dominerande transduktionsmekanismen tillskrevs piezoresistiviteten. En enorm skenbar effekt  $g \sim 6000$  med stark korrelation till enkelhålstunnling uppskattades utifrån våra mätningar. Denna hybridanordning är lovande för att kunna undersöka makroskopiskt kvantbeteende för vibrationsfononläge.

5. Symmetriska laterala bipolära transistorer (LBJT) tillverkades på SOI-skivor som lokala strömförstärkare för elektroniska SiNW-sensorer. Med basbredden 50 nm kunde en strömförstärkning på cirka 70 uppnås med god tillförlitlighet. För en  $n^+$ -p- $n^+$  typ av LBJT observerades en förbättring av strömförstärkning en positiv substratspänning, vilket skulle kunna förbättra EB-ströminjektionen nära Si/BOX gränssnittet. Emellertid ökar transportörens slumpmässiga infångning och avskärmning i närheten av Si/BOX gränssnittet LBJT bruset när gränssnittsströmmens bidrag till  $I_C$  är betydande. Att tillämpa en lämplig substratspänning kan både förbättra strömförstärkning av LBJT och uppnå en optimal total SNR.



# Acknowledgement

First and foremost, I want to show my deepest gratitude to my main supervisor Prof. Zhen Zhang. Thank you so much for providing me with the opportunity to study at Uppsala University and for your strong and professional support and guidance during my PhD period. You always inspire me to be positive and encourage me to fight against difficulties in the research. Thank you for supporting me to move forwards. I cannot complete the work in this thesis without your supervision!

I would like to thank my co-supervisor Dr. Si Chen. Thank you for your helpful and patient guidance and discussion on my research and study in the past five years. I am grateful for your erudite knowledge and rich experience. I also want to express my appreciation to my co-supervisor Prof. Shi-Li Zhang. I am inspired by your lasting passion and serious attitude towards science. I learn a lot from your broad and profound knowledge in physics, electronics, and language.

Particularly, I am grateful for Dr. Paul Solomon for your kind and tremendous support on my research. You are a so knowledgeable and serious scientist. I cannot forget your great help and patient discussion on fundamentals of semiconductor devices, measurement techniques, and physics models. Your insightful comments on my projects and the manuscripts really play a significant role.

I want to sincerely thank all the people involved in the SiNW projects. Thank you, Dr. Nathan L. Netzer and Prof. Zhenqiang Wang. I am grateful for your help in membrane preparation and ISE fabrication, and fruitful discussion on the manuscripts. Thank you, Dr. Zhuozhi Zhang and Prof. Guoping Guo, for the pleasant and sincere cooperation on the SiNW resonator project. I am deeply impressed by your erudite knowledge in quantum physics, experienced skills of cryogenic and RF measurements, and spirit of perseverance. Thank you, Prof. Hans Norström. Your great guidance and helpful discussion on the LBJT design, fabrication, and measurements were really important for me. The LBJT devices couldn't work in the first batch without your support.

Many thanks are also given to the persons who helped me in my PhD research and study. Thank you, Prof. Daniel Primetzhof, for the discussion and assistance on the ion implantation. Thank you, Prof. Leif Nyholm. We had fruitful discussion on solid/liquid interface, and I learnt much from you in the course of thin film deposition. Thank you, Prof. Carl Hägglund, for your

help in ALD process and ellipsometer measurements. I also learnt a lot in your course of thin film characterization. Thank you, Prof. Jörgen Olsson, for the discussion and assistance on RF pad design and RF measurements. I am impressed by your comments and suggestions of the LBJT characterization. Thank you, Prof. Tomas Kubart, for screening my thesis and giving me many useful comments. Your course really passed on much knowledge of fabrication processes. Thank you, Dr. Örjan Vallin. Your help in EBL and vertical furnace were so prompt. Thank you, Dr. Rimantas Brucas, for your nice suggestions on carrier wafer lithography. Thank you, Dr. Björn Kuzavas. You helped us a lot in building gas measurement setup. Thank you, Dr. Lars Riekehr. I couldn't get the XTEM images without your help. Thank you, Dr. Farhad Zamany, for your great support on wet etching process. In addition, I remember the support I got in Electrum. I want to say thanks to Prof. Per-Erik Hellström and Dr. Yongbin Wang for helping me when I met troubles of P5000. I also want to thank Dr. Ahmad Abedin and Laura Zurauskaite for your kind help and your experience on Epsilon 2000 and the RTP tool.

A deep gratitude is given to all group members. I cannot forget the help in both work and life I got from you. Now, all I can say is thanks to Da Zhang, Lukas Jablonka, Xingxing Xu, Shuangshuang Zeng, Yingtao Yu, Yuan Zhu, Zheqiang Xu, Chiao-Wei Tseng, Jiyue Wu, Indrek Must, Asta Makaraviciute, Quentin Palomar, Umut Cindemir, Yifei Liu, Elis Nycander.

I would also like to thank my colleagues and friends in the devision. Thank you, Ramy Salameh and Ida Näslund, for your much help in ordering products. Thank you, Ingrid Ringård and Linn Eriksson, for your kind help in visa application and employment contract. I also want to thank Jie Zhao, Shiyu Li, Chenyu Wen, Ruixue Zeng, Libo Chen, Ya Hu, Man Song, Ngan Pham, Zhibin Zhang, Renbin Tong, Wei-Chao Chen, Yao Yao, Yupeng Yang, Malkolm Hinnemo, Weiness Zhao, Michelle Marie Villamayor, Tobias Törndahl, Uwe Zimmermann, Long Hoang Duc, *etc.*

I want to thank my friends in Sweden for the great time we spent together in photography, badminton, bicycling, travelling, and hiking. Thank you, Xiaofeng Zhao, Ruijun Pan, Qiuhong Wang, Lei Tian, Rui Sun, Huan Wang, Xueying Kong, Pei Fu, Shengyang Zhou, Zhenghua Liu, Shuo Zhang, Bei Wang, Tianbo Duan, Yunbin Shen, Han Chen, Jingyi Yu, Wensong Bai, Mingzhi Jiao, Kai Song, Yanshuang Li, Chi Zhang, Ye Zou, Weian Sun, *etc.*

Acknowledge is given to the financial support from the Swedish Strategic Research Foundation, the Swedish Research Council, and the Wallenberg Academy Fellow Program.

最后，我要感谢我最亲爱的爸妈，感谢你们一直以来给予我的毫无保留的理解与支持，我将带着你们的爱继续向前！

Qitao Hu  
胡奇涛

2021-4-8, Uppsala

# References

1. A. A. Ensafi, "An introduction to sensors and biosensors," In *Electrochemical Biosensors*, 1st ed.; Ensafi, A.A., Ed.; Elsevier: Cambridge, MA, USA, 2019; pp. 1–10.
2. V. Naresh and N. Lee, "A review on biosensors and recent development of nanostructured materials-enabled biosensors," *Sensors*, vol. 21, no. 4, p. 1109, Feb. 2021.
3. Y. Moser and M. A. M. Gijs, "Miniaturized flexible temperature sensor," *IEEE J. Microelectromech. S.*, vol. 16, no. 6, pp. 1349–1354, Dec. 2007.
4. Y. Zhu and A. Wang, "Miniature fiber-optic pressure sensor," *IEEE Photonics Technol. Lett.*, vol. 17, no. 2, pp. 447–449, Feb. 2005.
5. Q. Kuang, C. Lao, Z. L. Wang, Z. Xie, and L. Zheng, "High-sensitivity humidity sensor based on a single SnO<sub>2</sub> nanowire," *J. Am. Chem. Soc.*, vol. 129, no. 19, pp. 6070–6071, Apr. 2007.
6. P. K. Ang, W. Chen, A. T. S. Wee, and K. P. Loh, "Solution-gated epitaxial graphene as pH sensor," *J. Am. Chem. Soc.*, vol. 130, no. 44, pp. 14392–14393, Oct. 2008.
7. M. Tantama, Y. P. Hung, and G. Yellen, "Imaging intracellular pH in live cells with a genetically encoded red fluorescent protein sensor," *J. Am. Chem. Soc.*, vol. 133, no. 26, pp. 10034–10037, Jun. 2011.
8. J. Zhang, S. Song, L. Wang, D. Pan, and C. Fan, "A gold nanoparticle-based chronocoulometric DNA sensor for amplified detection of DNA," *Nat. Protoc.*, vol. 2, pp. 2888–2895, Nov. 2007.
9. B. Sharma, A. Sharma, and J.-S. Kim, "Recent advances on H<sub>2</sub> sensor technologies based on MOX and FET devices: A review," *Sens. Actuators, B*, vol. 262, pp. 758–770, Jun. 2018.
10. H. G. Sudibya, Q. He, H. Zhang, and P. Chen, "Electrical detection of metal ions using field-effect transistors based on micropatterned reduced graphene oxide films," *ACS Nano*, vol. 5, no. 3, pp. 1990–1994, Feb. 2011.
11. J. Chaste, A. Eichler, J. Moser, G. Ceballos, R. Rurali, and A. Bachtold, "A nanomechanical mass sensor with yoctogram resolution," *Nat. Nanotechnol.*, vol. 7, pp. 301–344, May 2012.
12. J. R. Askima, M. Mahmoudiab, and K. S. Suslick, "Optical sensor arrays for chemical sensing: the optoelectronic nose," *Chem. Soc. Rev.*, vol. 42, pp. 8649–8682, Oct. 2013.
13. A. Yu, Z. Liang, J. Cho, and F. Caruso, "Nanostructured electrochemical sensor based on dense gold nanoparticle films," *Nano Lett.*, vol. 3, no. 9, pp. 1203–1207, Aug. 2003.
14. D. T. Quang and J. S. Kim, "Fluoro- and chromogenic chemodosimeters for heavy metal ion detection in solution and biospecimens," *Chem. Rev.*, vol. 110, no. 10, pp. 6280–6301, Aug. 2010.

15. Z. Altintas, "Surface plasmon resonance based sensor for the detection of glycopeptide antibiotics in milk using rationally designed nanoMIPs," *Sci. Rep.*, vol. 8, p. 11222, Jul. 2018.
16. P. A. Pandey, N. R. Wilson, and J. A. Covington, "Pd-doped reduced graphene oxide sensing films for H<sub>2</sub> detection," *Sens. Actuators, B*, vol. 183, pp. 478–487, Jul. 2013.
17. Y. Ma, M. Richards, M. Ghanem, Y. Guo, and J. Hassard, "Air pollution monitoring and mining based on sensor grid in London," *Sensors*, vol. 8, no. 6, pp. 3601–3623, Jun. 2008.
18. B. Reddy Jr, U. Hassan, C. Seymour, D. C. Angus, T. S. Isbell, K. White, W. Weir, L. Yeh, A. Vincent, and R. Bashir, "Point-of-care sensors for the management of sepsis," *Nat. Biomed. Eng.*, vol. 2, pp. 640–648, Sept. 2008.
19. Z. Yu, Y. Tang, G. Cai, R. Ren, and D. Tang, "Paper electrode-based flexible pressure sensor for point-of-care immunoassay with digital multimeter," *Anal. Chem.*, vol. 91, no. 2, pp. 1222–1226, Dec. 2018.
20. L. Mainetti, L. Patrono, and A. Vilei, "Evolution of wireless sensor networks towards the Internet of Things: A survey," in *19<sup>th</sup> Int. Conf. Softw., Telecommun. Comput. Netw. (SoftCOM)*, pp. 1–6, Sept. 2011.
21. P. Bergveld, "Development of an ion-sensitive solid-state device for neurophysiological measurements," *IEEE Trans. Biomed. Eng.*, vol. BME-17, no. 1, pp. 70–71, Jan. 1970.
22. M. J. Schoning and A. Poghossian, "Recent advances in biologically sensitive field-effect transistors (BioFETs)," *Analyst*, vol. 127, no. 9, pp. 1137–1151, Aug. 2002.
23. P. Bergveld, "Thirty years of ISFETOLOGY: What happened in the past 30 years and what may happen in the next 30 years," *Sens. Actuators, B*, vol. 88, no. 1, pp. 1–20, Jan. 2003.
24. Y. Cui, Q. Wei, H. Park, and C. M. Lieber, "Nanowire nanosensors for highly sensitive and selective detection of biological and chemical species," *Science*, vol. 293, no. 5533, pp. 1289–1292, Aug. 2001.
25. S. Chen, J. G. Bomer, E. T. Carlen, and A. van den Berg, "Al<sub>2</sub>O<sub>3</sub>/silicon nanoISFET with near ideal Nernstian response," *Nano Lett.*, vol. 11, no. 6, pp. 2334–2341, Apr. 2011.
26. M. Wipf, R. L. Stoop, A. Tarasov, K. Bedner, W. Fu, I. A. Wright, C. J. Martin, E. C. Constable, M. Calame, and C. Schönenberger, "Selective sodium sensing with gold-coated silicon nanowire field-effect transistors in a differential setup," *ACS Nano*, vol. 7, no. 7, pp. 5978–5983, Jun. 2013.
27. O. Knopfmacher, A. Tarasov, W. Fu, M. Wipf, B. Niesen, M. Calame, and C. Schönenberger, "Nernst limit in dual-gated Si-nanowire FET sensors," *Nano Lett.*, vol. 10, no. 6, pp. 2268–2274, May 2010.
28. E. Stern, J. F. Klemic, D. A. Routenberg, P. N. Wyrembak, D. B. Turner-Evans, A. D. Hamilton, D. A. LaVan, T. M. Fahmy, and M. A. Reed, "Label-free immunodetection with CMOS-compatible semiconducting nanowires," *Nature*, vol. 445, pp. 519–522, Feb. 2007.
29. Y. L. Bunimovich, Y. S. Shin, W.-S. Yeo, M. Amori, G. Kwong, and J. R. Heath, "Quantitative real-time measurements of DNA hybridization with alkylated nonoxidized silicon nanowires in electrolyte solution," *J. Am. Chem. Soc.*, vol. 128, no. 50, pp. 16323–16331, Dec. 2006.
30. J. H. Chua, R.-E. Chee, A. Agarwal, S. M. Wong, and G.-J. Zhang, "Label-free electrical detection of cardiac biomarker with complementary metal-oxide semiconductor-compatible silicon nanowire sensor arrays," *Anal. Chem.*, vol. 81, no. 15, pp. 6266–6271, Jul. 2009.

31. B. Wang, J. C. Cancilla, J. S. Torrecilla, and H. Haick, "Artificial sensing intelligence with silicon nanowires for ultraselective detection in the gas phase," *Nano Lett.*, vol. 14, no. 2, pp. 933–938, Jan. 2014.
32. Y. Engel, R. Elnathan, A. Pevzner, G. Davidi, E. Flaxer, and F. Patolsky, "Supersensitive detection of explosives by silicon nanowire arrays," *Angew. Chem. Int. Ed.*, vol. 122, no. 38, pp. 6982–6987, Sept. 2010.
33. A. Gao, X. Yang, J. Tong, L. Zhou, Y. Wang, J. Zhao, H. Mao, and T. Li, "Multiplexed detection of lung cancer biomarkers in patients serum with CMOS-compatible silicon nanowire arrays," *Biosens. Bioelectron.*, vol. 91, no. 15, pp. 482–488, May 2017.
34. J.-Y. Kim, J.-H. Ahn, D.-I. Moon, T. J. Park, S. Y. Lee, and Y.-K. Choia, "Multiplex electrical detection of avian influenza and human immunodeficiency virus with an underlap-embedded silicon nanowire field-effect transistor," *Biosens. Bioelectron.*, vol. 55, no. 15, pp. 162–167, May 2014.
35. B. He, T. J. Morrow, and C. D. Keating, "Nanowire sensors for multiplexed detection of biomolecules," *Curr. Opin. Chem. Biol.*, vol. 12, no. 5, pp. 522–528, Oct. 2008.
36. G. Zheng, F. Patolsky, Y. Cui, W. U. Wang, and C. M. Lieber, "Multiplexed electrical detection of cancer markers with nanowire sensor arrays," *Nat. Biotechnol.*, vol. 23, pp. 1294–1301, Sept. 2005.
37. N. K. Rajan, D. A. Routenberg, and M. A. Reed, "Optimal signal-to-noise ratio for silicon nanowire biochemical sensors," *Appl. Phys. Lett.*, vol. 98, p. 264107, Jul. 2011.
38. N. Clément, K. Nishiguchi, J. F. Dufreche, D. Guerin, A. Fujiwara, and D. Vuillaume, "A Si nanowire ion-sensitive field-effect transistor with elementary charge sensitivity," *Appl. Phys. Lett.*, vol. 98, p. 014104, Jan. 2011.
39. G. He, J. Li, H. Ci, C. Qi, and X. Guo, "Direct measurement of single-molecule DNA hybridization dynamics with single-base resolution," *Angew. Chem. Int. Ed.*, vol. 128, no. 31, pp. 9182–9186, Jul. 2016.
40. S. Sorgenfrei, C. Chiu, R. L. Gonzalez, Jr, Y.-J. Yu, P. Kim, C. Nuckolls, and K. L. Shepard, "Label-free single-molecule detection of DNA hybridization kinetics with a carbon nanotube field-effect transistor," *Nat. Nanotechnol.*, vol. 6, pp. 126–132, Jan. 2011.
41. S. Sorgenfrei, C. Chiu, M. Johnston, C. Nuckolls, and K. L. Shepard, "Debye screening in single-molecule carbon nanotube field-effect sensors," *Nano Lett.*, vol. 11, no. 9, pp. 3739–3743, Aug. 2011.
42. Y. Yang, L. Ding, J. Han, Z. Zhang, and L.-M. Peng, "High-performance complementary transistors and medium-scale integrated circuits based on carbon nanotube thin films," *ACS Nano*, vol. 11, no. 4, pp. 4124–4132, Mar. 2017.
43. C. Leung, H. Kinns, B. W. Hoogenboom, S. Howorka, and P. Mesquida, "Imaging surface charges of individual biomolecules," *Nano Lett.*, vol. 9, no. 7, pp. 2769–2773, Jun. 2009.
44. Y. Wen, N. Ares, F. J. Schupp, T. Pei, G. A. D. Briggs, and E. A. Laird, "A coherent nanomechanical oscillator driven by single-electron tunnelling," *Nat. Phys.*, vol. 16, pp. 75–82, Jan. 2020.
45. F. A. Zwanenburg, A. S. Dzurak, A. Morello, M. Y. Simmons, L. C. L. Hollenberg, G. Klimeck, S. Rogge, S. N. Coppersmith, and M. A. Eriksson, "Silicon quantum electronics," *Rev. Mod. Phys.*, vol. 85, no. 3, pp. 961–1019, Sept. 2013.

46. C. H. Yang, R. C. C. Leon, J. C. C. Hwang, A. Saraiva, T. Tanttu, W. Huang, J. Camirand Lemyre, K. W. Chan, K. Y. Tan, F. E. Hudson, K. M. Itoh, A. Morello, M. Pioro-Ladrière, A. Laucht, and A. S. Dzurak, "Operation of a silicon quantum processor unit cell above one kelvin," *Nature*, vol. 580, pp. 350–354, Apr. 2020.
47. J. B. Clark, F. Lecocq, R. W. Simmonds, J. Aumentado, and J. D. Teufel, "Sideband cooling beyond the quantum backaction limit with squeezed light," *Nature*, vol. 541, pp. 191–195, Jan. 2017.
48. Y. Chu, P. Kharel, T. Yoon, L. Frunzio, P. T. Rakich, and R. J. Schoelkopf, "Creation and control of multi-phonon Fock states in a bulk acoustic-wave resonator," *Nature*, vol. 563, pp. 666–670, Nov. 2018.
49. A. Casnati, A. Pochini, R. Ungaro, C. Bocchi, F. Uguzzoli, R. J. M. Egberink, H. Struijk, R. Lugtenberg, F. D. Jong, and D. N. Reinhoudt, "1,3-alternate calix[4]arene-crown-5 conformers: new synthetic ionophores with better  $K^+/Na^+$  selectivity than valinomycin," *Chem. Eur. J.*, vol. 2, no. 4, pp. 436–445, Apr. 1996.
50. K. Suzuki, K. Sato, H. Hisamoto, D. Siswanta, K. Hayashi, N. Kasahara, K. Watanabe, N. Yamamoto, and H. Sasakura, "Design and synthesis of sodium ion-selective ionophores based on 16-crown-5 derivatives for an ion-selective electrode," *Anal. Chem.*, vol. 68, no. 1, pp. 208–215, Jan. 1996.
51. C. Staii, A. T. Johnson, M. Chen, and A. Gelperin, "DNA-decorated carbon nanotubes for chemical sensing," *Nano Lett.*, vol. 5, no. 9, pp. 1774–1778, Aug. 2005.
52. A. Bratov, N. Abramova, and C. Domínguez, "Investigation of chloride sensitive ISFETs with different membrane compositions suitable for medical applications," *Anal. Chim. Acta*, vol. 514, no. 1, pp. 99–106, Jun. 2004.
53. N. C. S. Vieira, E. G. R. Fernandes, A. D. Faceto, V. Zucolotto, and F. E. G. Guimaraes, "Nanostructured polyaniline thin films as pH sensing membranes in FET-based devices," *Sens. Actuators, B*, vol. 160, pp. 312–317, Aug. 2011.
54. R. E. G. van Hal, J. C. T. Eijkel, and P. Bergveld, "A novel description of ISFET sensitivity with the buffer capacity and double-layer capacitance as key parameters," *Sens. Actuators, B*, vol. 24, no. 1–3, pp. 201–205, Mar. 1995.
55. O. Stern, "Zur theorie der elektrolytischen doppelschicht," *Zeitschrift für Elektrochemie und Angewandte Physikalische Chemie*, vol. 30, no. 21–22, pp. 508–516, Nov. 1924.
56. M. M. Walczak, D. A. Dryer, D. D. Jacobson, M. G. Foss, and N. T. Flynn, "pH dependent redox couple: an illustration of the Nernst equation," *J. Chem. Educ.*, vol. 74, no. 10, p. 1195, Oct. 1997.
57. R. E. G. van Hal, J. C. T. Eijkel, and P. Bergveld, "A general model to describe the electrostatic potential at electrolyte oxide interfaces," *Adv. Colloid Interface Sci.*, vol. 69, no. 1–3, pp. 31–62, Dec. 1996.
58. S. D. Suk, S.-Y. Lee, S.-M. Kim, E.-J. Yoon, M.-S. Kim, M. Li, C. W. Oh, K. H. Yeo, S. H. Kim, D.-S. Shin, K.-H. Lee, H. S. Park, J. N. Han, C. J. Park, J.-B. Park, D.-W. Kim, D. Park, and B.-I. Ryu, "High performance 5nm radius Twin Silicon Nanowire MOSFET (TSNWFET): fabrication on bulk Si wafer, characteristics, and reliability," in *IEEE Int. Electron Devices Meeting, (IEDM)*, pp. 717–720, Dec. 2005.
59. S. T. Martin, G. P. Li, E. Worley, and J. White, "The gate bias and geometry dependence of random telegraph signal amplitudes," *IEEE Electron Device Lett.*, vol. 18, no. 9, pp. 444–446, Sept. 1997.

60. K. Shoorideh and C. O. Chui, "On the sensitivity of FET-based nanobiosensors," *Proc. Natl. Acad. Sci. U.S.A.*, vol. 111, no. 14, pp. 5111–5116, Apr. 2014.
61. N. V. Amarasinghe, Z. Celik-Butler, and A. Keshavarz, "Extraction of oxide trap properties using temperature dependence of random telegraph signals in submicron metal-oxide-semiconductor field-effect transistors," *J. Appl. Phys.*, vol. 89, no. 10, p. 5526, May 2001.
62. Z. Shi, J.-P. Mieveille, and M. Dutoit, "Random telegraph signals in deep submicron n-MOSFET's," *IEEE Trans. Electron Devices*, vol. 41, no. 7, pp. 1161–1168, Jul. 1994.
63. J. Li, S. Pud, M. Petrychuk, A. Offenhäusser, and S. Vitusevich, "Sensitivity enhancement of Si nanowire field-effect transistor biosensors using single trap phenomena," *Nano Lett.*, vol. 14, no. 6, pp. 3504–3509, May 2014.
64. K. L. Ekinici and M. L. Roukes, "Nanoelectromechanical systems," *Rev. Sci. Instrum.*, vol. 76, p. 061101, Apr. 2005.
65. A. Tokmakoff, B. Sauter, and M. D. Fayer, "Temperature-dependent vibrational relaxation in polyatomic liquids: Picosecond infrared pump-probe experiments," *J. Chem. Phys.*, vol. 100, p. 9035, Mar. 1994.
66. R. A. Norte, J. P. Moura, and S. Groblacher, "Mechanical resonators for quantum optomechanics experiments at room temperature," *Phys. Rev. Lett.*, vol. 116, p. 147202, Apr. 2016.
67. M. Poot and H. S. J. van der Zant, "Mechanical systems in the quantum regime," *Phys. Rep.*, vol. 511, no. 5, pp. 273–335, Feb. 2012.
68. J. Zhuge, R. Wang, R. Huang, Y. Tian, L. Zhang, D.-W. Kim, D. Park, Y. Wang, "Investigation of low-frequency noise in silicon nanowire MOSFETs," *IEEE Electron Device Lett.*, vol. 30, no. 1, pp. 57–60, Jan. 2009.
69. E. Simoen and C. Claeys, "On the flicker noise in submicron silicon MOSFETs," *Solid-State Electron.*, vol. 43, no. 5, pp. 865–882, May 1999.
70. S. Zafar, C. D'Emic, A. Jagtiani, E. Kratschmer, X. Miao, Y. Zhu, R. Mo, N. Sosa, H. Hamann, G. Shahidi, and H. Riel, "Si nanowire field effect transistor sensors with minimal sensor-to-sensor variations and enhanced sensing characteristics," *ACS nano*, vol. 12, no. 7, pp. 6577–6587, Jun. 2018.
71. D. Zhang, X. Gao, S. Chen, H. Norström, U. Smith, P. Solomon, S.-L. Zhang, and Z. Zhang, "An ion-gated bipolar amplifier for ion sensing with enhanced signal and improved noise performance," *Appl. Phys. Lett.*, vol. 105, no. 8, p. 082102, Aug. 2014.
72. A. E. Grigorescu and C. W. Hagen, "Resists for sub-20-nm electron beam lithography with a focus on HSQ: state of the art," *Nanotechnology*, vol. 20, no. 29, p. 292001, Jul. 2009.
73. T. H. P. Chang, "Proximity effect in electron-beam lithography," *J. Vac. Sci. Technol.*, vol. 12, no. 6, p. 1271, Nov. 1975.
74. A. T. Ping, Q. Chen, J. W. Yang, M. Asif Khan, and I. Adesida, "The effects of reactive ion etching-induced damage on the characteristics of ohmic contacts to n-type GaN," *J. Electron. Mater.*, vol. 27, pp. 261–265, Apr. 1998.
75. S. Bangsaruntip, G. M. Cohen, A. Majumdar, Y. Zhang, S. U. Engelmann, N. C. M. Fuller, L. M. Gignac, S. Mittal, J. S. Newbury, M. Guillorn, T. Barwicz, L. Sekaric, M. M. Frank, and J. W. Sleight, "High performance and highly uniform gate-all-around silicon nanowire MOSFETs with wire size dependent scaling," in *IEEE Int. Electron Devices Meeting, (IEDM)*, pp. 1–4, Dec. 2009.
76. K. Martens, S. Santermans, M. Gupta, G. Hellings, R. Wuytens, B. Du Bois, E. Dupuy, E. Altamirano-Sanchez, K. Jans, R. Vos, T. Stakenborg, L. Lagae, M. Heyns, S. Severi, and W. Van Roy, "BioFET technology: aggressively

- scaled pMOS FinFET as biosensor,” in *IEEE Int. Electron Devices Meeting, (IEDM)*, pp. 18.6.1–18.6.4, Dec. 2019.
77. F.-R. Dai and Z. Wang, “Modular assembly of metal–organic supercontainers incorporating sulfonycalixarenes,” *J. Am. Chem. Soc.*, vol. 134, no. 19, pp. 8002–8005, May 2012.
  78. E. Bakker, P. Bühlmann, and E. Pretsch, “Carrier-based ion-selective electrodes and bulk optodes. 1. general. characteristics,” *Chem. Rev.*, vol. 97, no. 8, pp. 3083–3132, Dec. 1997.
  79. S. Ogawara, J. L. Carey, X. U. Zou, and P. Buhlmann, “Donnan failure of ion-selective electrodes with hydrophilic high-capacity ion-exchanger membranes,” *ACS Sens.*, vol. 1, no. 1, pp. 95–101, Nov. 2015.
  80. J. A. J. Brunink, J. G. Bomer, J. F. J. Engbersen, W. Verboom, and D. N. Reinhoudt, “Effects of anionic sites on the selectivity of sodium-sensitive CHEMFETs,” *Sens. and Actuators, B*, vol. 15, no. 1–3, pp. 195–198, Aug. 1993.
  81. S. Wongchitphimon, R. Wang, R. Jiratananon, L. Shi, C.H. Loh, “Effect of polyethylene glycol [PEG] as an additive on the fabrication of polyvinylidene fluoride-co-hexafluoropropylene [PVDF-HFP] asymmetric microporous hollow fiber membranes,” *J. Membr. Sci.*, vol. 369, no. 1–2, pp. 329–338, Mar. 2011.
  82. Y.-H. Zhao, B.-K. Zhu, X.-T. Ma, and Y.-Y. Xu, “Porous membranes modified by hyperbranched polymers: I. Preparation and characterization of PVDF membrane using hyperbranched polyglycerol as additive,” *J. Membr. Sci.*, vol. 290, no. 1–2, pp. 222–229, Mar. 2007.
  83. N. L. Netzer, I. Must, Y. Qiao, S.-L. Zhang, Z. Wang, and Z. Zhang, “Biomimetic supercontainers for size-selective electrochemical sensing of molecular ions,” *Sci. Rep.*, vol. 7, p. 45786, Apr. 2017.
  84. G. W. Trucks, Krishnan Raghavachari, G. S. Higashi, and Y. J. Chabal, “Mechanism of HF etching of silicon surfaces: A theoretical understanding of hydrogen passivation,” *Phys. Rev. Lett.*, vol. 65, p. 504, Jul. 1990.
  85. E. Yablonovitch, D. L. Allara, C. C. Chang, T. Gmitter, and T. B. Bright, “Unusually low surface-recombination velocity on silicon and germanium surfaces,” *Phys. Rev. Lett.*, vol. 57, p. 249, Jul. 1986.
  86. M. Banaszkeski da Silva, H. P. Tuinhout, A. Zegers-van Duijnhoven, G. I. Wirth and A. J. Scholten, “A physics-based statistical RTN model for the low frequency noise in MOSFETs,” *IEEE Trans. Electron Devices*, vol. 63, no. 9, pp. 3683–3692, Sept. 2016.
  87. P. M. Lenahan, T. D. Mishima, J. Jumper, T. N. Fogarty, and R. T. Wilkins, “Direct experimental evidence for atomic scale structural changes involved in the interface-trap transformation process,” *IEEE Trans. Nucl. Sci.*, vol. 48, no. 6, pp. 2131–2135, Dec. 2001.
  88. M. J. Kirton and M. J. Uren, “Noise in solid state microstructures: a new perspective on individual defects, interface states and low-frequency (1/f) noise,” *Adv. Phys.*, vol. 38, no. 4, pp. 367–468, Nov. 1989.
  89. M. Si, N. J. Conrad, S. Shin, J. Gu, J. Zhang, M. A. Alam, P. D. Ye, “Low-Frequency Noise and Random Telegraph Noise on Near-Ballistic III-V MOSFETs,” *IEEE Trans. Electron Devices*, vol. 62, no. 11, pp. 3508–3515, Nov. 2015.
  90. Y. Liu and L. Shen, “From Langmuir kinetics to first- and second-order rate equations for adsorption,” *Langmuir*, vol. 24, no. 20, pp. 11625–11630, Sept. 2008.



91. K. K. Hung, P. K. Ko, C. Hu, and Y. C. Cheng, "A unified model for the flicker noise in metal-oxide-semiconductor field-effect transistors," *IEEE Trans. Electron Devices*, vol. 37, no. 3, pp. 654–665, Mar. 1990.
92. N. Clément, K. Nishiguchi, A. Fujiwara, and D. Vuillaume, "One-by-one trap activation in silicon nanowire transistors," *Nat. Commun.*, vol. 1, p. 92, Oct. 2010.
93. S. Manzeli, D. Dumcenco, G. M. Marega, and A. Kis, "Self-sensing, tunable monolayer MoS<sub>2</sub> nanoelectromechanical resonators," *Nat. Commun.*, vol. 10, p. 4831, Oct. 2019.
94. A. Eichler, J. Moser, J. Chaste, M. Zdrojek, I. Wilson-Rae, and A. Bachtold, "Nonlinear damping in mechanical resonators made from carbon nanotubes and graphene," *Nat. Nanotechnol.*, vol. 6, pp. 339–342, May 2011.
95. F. A. Zwanenburg, C. E. W. M. van Rijmenam, Y. Fang, C. M. Lieber, and L. P. Kouwenhoven, "Spin states of the first four holes in a silicon nanowire quantum dot," *Nano Lett.*, vol. 9, no. 3, pp. 1071–1079, Feb. 2009.
96. Z.-Z. Zhang, X.-X. Song, G. Luo, Z.-J. Su, K.-L. Wang, G. Cao, H.-O. Li, M. Xiao, G.-C. Guo, L. Tian, G.-W. Deng, and G.-P. Guo, "Coherent phonon dynamics in spatially separated graphene mechanical resonators," *Proc. Natl. Acad. Sci. U.S.A.*, vol. 117, no. 11, pp. 5582–5587, Mar. 2020.
97. B. Lassagne, Y. Tarakanov, J. Kinaret, D. Garcia-Sanchez, and A. Bachtold, "Coupling mechanics to charge transport in carbon nanotube mechanical resonators," *Science*, vol. 325, no. 5944, pp. 1107–1110, Aug. 2009.
98. R. He and P. Yang, "Giant piezoresistance effect in silicon nanowires," *Nat. Nanotechnol.*, vol. 1, pp. 42–46, Oct. 2006.
99. M. M. McClarty, N. Jegenyess, M. Gaudet, C. Toccafondi, R. Ossikovski, F. Vaurette, S. Arscott, and A. C. H. Rowe, "Geometric and chemical components of the giant piezoresistance in silicon nanowires," *Appl. Phys. Lett.*, vol. 109, no. 2, p. 023102, Jul. 2016.
100. A. Koumela, D. Mercier, C. Dupré, G. Jourdan, C. Marcoux, E. Ollier, S. T. Purcell, and L. Duraffourg, "Piezoresistance of top-down suspended Si nanowires," *Nanotechnology*, vol. 22, no. 39, p. 395701, Sept. 2011.
101. P. Neuzil, C. C. Wong, J. Reboud, "Electrically controlled giant piezoresistance in silicon nanowires," *Nano Lett.*, vol. 10, no. 4, pp. 1248–1252, Mar. 2010.
102. P. Hashemi, J.-B. Yau, K. K. Chan, T. H. Ning, and G. G. Shahidi, "Demonstration of symmetric lateral NPN transistors on SOI featuring epitaxially grown emitter/collector regions," *IEEE J. Electron Devices Soc.*, vol. 6, pp. 537–542, Dec. 2017.
103. J. A. Babcock, D. K. Schroder, W.-L. M. Huang, and J. M. Ford, "Low-frequency noise in TFSOI lateral N-P-N bipolar transistors," *IEEE Trans. Electron Devices*, vol. 48, no. 5, pp. 956–965, May 2001.
104. M. J. Deen and E. Simoen, "Low-frequency noise in polysilicon-emitter bipolar transistors," *IET Circuits Devices Syst.*, vol. 149, no. 1, pp. 40–50, Feb. 2002.
105. C. G. Theodorou, E. G. Ioannidis, F. Andrieu, T. Poiroux, O. Faynot, C. A. Dimitriadis, and G. Ghibaudo, "Low-frequency noise sources in advanced UTBB FD-SOI MOSFETs," *IEEE Trans. Electron Devices*, vol. 61, no. 4, pp. 1161–1167, Apr. 2014.
106. K. K. Hung, P. K. Ko, C. Hu, and Y. C. Cheng, "A unified model for the flicker noise in metal-oxide-semiconductor field-effect transistors," *IEEE Trans. Electron Devices*, vol. 37, no. 3, pp. 654–665, Mar. 1990.

# Acta Universitatis Upsaliensis

*Digital Comprehensive Summaries of Uppsala Dissertations  
from the Faculty of Science and Technology 2032*

Editor: The Dean of the Faculty of Science and Technology

A doctoral dissertation from the Faculty of Science and Technology, Uppsala University, is usually a summary of a number of papers. A few copies of the complete dissertation are kept at major Swedish research libraries, while the summary alone is distributed internationally through the series Digital Comprehensive Summaries of Uppsala Dissertations from the Faculty of Science and Technology. (Prior to January, 2005, the series was published under the title "Comprehensive Summaries of Uppsala Dissertations from the Faculty of Science and Technology".)



ACTA  
UNIVERSITATIS  
UPSALIENSIS  
UPPSALA  
2021

Distribution: [publications.uu.se](http://publications.uu.se)  
urn:nbn:se:uu:diva-439645